1   **Delayed induction of type I and III interferons mediates nasal epithelial cell permissiveness**

2   **to SARS-CoV-2**

3

4   *Nasal interferon responses to SARS-CoV-2*

5

6   **Authors**

7   Catherine F Hatton[1a], Rachel A Botting[2a], Maria Emilia Dueñas[2a], Iram J Haq[1,3a], Bernard Verdon[2a],

8   Benjamin J Thompson[1], Jarmila Stremenova Spegarova[1], Florian Gothe[1,4], Emily Stephenson[2], Aaron I

9   Gardner[1], Sandra Murphy[2], Jonathan Scott[1], James P Garnett[1], Sean Carrie[5], Jason Powell[1], C M Anjam

10   Khan[2], Lei Huang[1], Rafiqul Hussain[6], Jonathan Coxhead[6], Tracey Davey[7], A John Simpson[1], Muzlifah

11   Haniffa[2,8,9,10], Sophie Hambleton[1,11], Malcolm Brodlie[1,3b], Chris Ward[1b], Matthias Trost[2b], Gary

12   Reynolds[2b], Christopher J A Duncan[1,12 b]*

13

14   [a] equal contribution

15   [b] equal contribution

16   * corresponding author: christopher.duncan@ncl.ac.uk

17

18   **Affiliations**

19   1. Translational and Clinical Research Institute, Faculty of Medical Sciences, Newcastle University,

20   Newcastle upon Tyne, UK.

21   2. Biosciences Institute, Newcastle University, Newcastle upon Tyne, UK.

22   3. Paediatric Respiratory Medicine, Great North Children's Hospital, Newcastle upon Tyne Hospitals

23   NHS Foundation Trust, Newcastle upon Tyne, UK.

24   4. Department of Pediatrics, Dr. von Hauner Children's Hospital, University Hospital, Ludwig-

25   Maximilians-Universität Munich, Munich, Germany.

26   5. Population Health Sciences Institute, Newcastle University, Newcastle upon Tyne, UK.

27   6. Genomics Core Facility, Biosciences Institute, Newcastle University, Newcastle upon Tyne, UK.

28   7. Electron Microscopy Research Services, Newcastle University, Newcastle upon Tyne, UK.

29   8. NIHR Newcastle Biomedical Research Centre, Newcastle Hospitals NHS Foundation Trust, Newcastle

30   upon Tyne, UK

31   9. Department of Dermatology, Newcastle Hospitals NHS Foundation Trust, Newcastle upon Tyne, UK

32   10. Wellcome Sanger Institute, Wellcome Genome Campus, Cambridge, UK

33   11. Great North Children's Hospital, Newcastle upon Tyne Hospitals NHS Foundation Trust, UK.

34   12. Department of Infection and Tropical Medicine, Newcastle upon Tyne Hospitals NHS Foundation

35   Trust, UK.

36

37   **Abstract**

38   The nasal epithelium is a plausible entry point for SARS-CoV-2, a site of pathogenesis and transmission,

39   and may initiate the host response to SARS-CoV-2. Antiviral interferon (IFN) responses are critical to

40   outcome of SARS-CoV-2. Yet little is known about the interaction between SARS-CoV-2 and innate

41   immunity in this tissue. Here we applied single-cell RNA sequencing and proteomics to a primary cell

42   model of human nasal epithelium differentiated at air-liquid interface. SARS-CoV-2 demonstrated

43   widespread tropism for nasal epithelial cell types. The host response was dominated by type I and III

44   IFNs and interferon-stimulated gene products. This response was notably delayed in onset relative to

45   viral gene expression and compared to other respiratory viruses. Nevertheless, once established, the

46   paracrine IFN response began to impact on SARS-CoV-2 replication. When provided prior to infection,

47   recombinant IFNβ or IFNλ1 induced an efficient antiviral state that potently restricted SARS-CoV-2

48   viral replication, preserving epithelial barrier integrity. These data suggest that the IFN-I/III response

49   to SARS-CoV-2 initiates in the nasal airway and suggest nasal delivery of recombinant IFNs to be a

50   potential chemoprophylactic strategy.

INTRODUCTION

SARS-CoV-2 is an emergent betacoronavirus responsible for coronavirus disease-19 (COVID-19)[1]. Since its identification in late 2019, global pandemic transmission of SARS-CoV-2 has resulted in over 192 million confirmed infections and approximately 4.1 million deaths. SARS-CoV-2 infects target cells via the entry receptor ACE2[2] leading to a spectrum of clinical outcomes, ranging from asymptomatic infection to death[3]. Although multiple host factors (e.g. age, male sex, obesity) contribute to adverse clinical outcome[4], the immune response also plays a decisive role, evidenced by the therapeutic benefit of immunomodulatory agents including corticosteroids[5] or IL6 inhibition[6]. Yet much remains to be understood about the immunopathogenesis of COVID-19. Identification of the cells hosting viral entry and characterisation of their response to infection is essential to understanding pathogenesis and improving therapy.

The nasal epithelium is believed to be a key entry point of SARS-CoV-2. Nasal epithelial tropism and efficient viral shedding from the nasopharynx apparently contributes to the high transmissibility of SARS-CoV-2[7], as well as to pathologic features such as anosmia[8]. As an early viral target cell, nasal epithelial cells may also set the tone for the systemic immune response, potentially influencing disease outcome[9]. These factors emphasise the need to study host-virus interaction in human nasal cells. *Ex vivo* single-cell transcriptomic studies indicate that ciliated and/or goblet cells in the nasal mucosa express *ACE2* and *TMPRSS2,* implicating them as probable SARS-CoV-2 target cells[10,11]. This has been confirmed by *in vitro* and *in vivo* studies demonstrating SARS-CoV-2 infection of human nasal epithelial cells[12-15]. Single-cell studies also revealed that nasal cells exhibit basal expression of an antiviral expression programme, characterised by induction of several interferon-stimulated genes (ISGs), suggesting that they may be primed to respond to viral infection[10,11]. Interestingly, *ACE2* is also regulated by interferons (IFNs)[11,16], implying a complex relationship between IFN signalling and tropism. Type I and type III IFN (IFN-I/III) systems play a critical role in human antiviral innate immunity[17] and have been recently implicated in defence against SARS-CoV-2 susceptibility to severe or life-threatening COVID-19 is associated with deleterious variants in *IFNAR* genes[18,19] and IFN-I

77 blocking autoantibodies[20]. *In vitro*, SARS-CoV-2 appears sensitive to the antiviral properties of IFN-I,

78 at least in cell lines[21,22], and this activity extends to *in vivo* model systems[9]. These findings motivate

79 studies to improve understanding of the interaction between SARS-CoV-2 and the IFN-I system in

80 primary human target cells, providing impetus to clinical trials of recombinant IFNs in treatment or

81 prophylaxis of COVID-19[23].

82 Organotypic cultures of primary human nasal epithelium differentiated at air-liquid interface (ALI) are

83 a translationally relevant primary cell model for studies of SARS-CoV-2 host-virus interaction[12], with

84 considerable potential to accelerate our understanding of pathogenesis. A small number of studies

85 using this model demonstrate that SARS-CoV-2 replicates efficiently in human nasal cells[12-14], yet

86 important questions concerning cellular tropism and their innate immune response remain

87 unresolved. Hou and colleagues report that only ciliated cells were permissive to SARS-CoV-2, despite

88 expression of ACE2 and TMPRSS2 by all cell types[13]. They hypothesised that post-entry factors, such

89 as innate immunity, might govern tropism. By contrast, Pizzorno and colleagues reported infection in

90 all major cell types (ciliated, secretory and basal cells)[14], consistent with prior indications from single-

91 cell RNA sequencing (scRNA-seq) data and studies in lower airway models[24,25]. While an IFN response

92 to SARS-CoV-2 can be detected in nasal cells[12,14], in apparent contrast to bronchial or alveolar

93 epithelial cells[26-28], the kinetics of induction and the antiviral function of IFNs in nasal epithelium has

94 not been systematically characterised.

95 Here we employed a comprehensive range of techniques, including scRNA-seq and proteomics, in

96 primary human nasal ALI cultures to define: (i) cellular tropism; (ii) the innate immune response to

97 SARS-CoV-2; and (iii) the antiviral activity of IFN-I/III. We observed broad cellular tropism of SARS-CoV-

98 2 for nasal epithelial cells, although secretory and ciliated cells were the most permissive. Nasal cells

99 mounted a delayed IFN response that began to exert control over viral replication at later times post-

100 infection. However, SARS-CoV-2 remained highly sensitive to IFN-restriction if exogenous IFN-I/III was

101 applied prior to infection. These data enrich our understanding of the interaction of SARS-CoV-2 and

102 the human IFN system at the earliest point of infection, with immediate therapeutic implications.

103

RESULTS

SARS-CoV-2 robustly infects primary differentiated nasal epithelial cultures

Primary nasal epithelial cultures were established from cryopreserved stocks from six adult donors, obtained prior to the SARS-CoV-2 pandemic. Cells were expanded, differentiated and then matured at ALI for 28 days, according to an established protocol[29]. We first sought to address their suitability as a model of SARS-CoV-2 infection. Single-cell RNA-seq libraries were generated from two representative donors, yielding 28,346 individual transcriptomes for analysis following quality control (Fig. S1, Table S1). Following dimensionality reduction and Leiden clustering, eight populations were discerned by their expression of established marker genes[11,30] (Fig. 1A, supplementary dataset 1). This annotation was further validated using Seurat label transfer from a published scRNA-seq dataset from nasopharyngeal swabs[15] (Fig. 1B). The major populations identified were ciliated, secretory, goblet and basal cells, alongside two rarer populations of FOXN4+ deuterosomal cells[31] and ionocytes. Cells expressed characteristic markers (Fig. 1C and supplementary dataset 1), corresponding closely to *ex vivo* single-cell data from nasal brusings[15] (Fig. 1B). Immunostaining verified the presence of major cell types in these cultures using well-established protein markers[13] - including acetylated alpha-tubulin-positive (AAT) ciliated cells, mucin 5B-positive (MUC5B) secretory cells, mucin 5AC (MUC5AC)-positive goblet cells, and tumour protein 63-positive (TP63) basal cells (Fig. S2) - with ciliated cells the most abundant cell population. Consistent with published scRNA-seq data[10,11,15], mRNA for key SARS-CoV-2 entry receptors, *ACE2* and *TMPRSS2*, was expressed, albeit at relatively low levels, alongside other genes implicated in SARS-CoV-2 entry such as *FURIN* and *CTSL* (Fig. S3)[32]. Robust expression of ACE2 and TMPRSS2 at the protein level was confirmed by immunoblotting of whole-cell lysates prepared from mature ALI cultures (Fig. 1D). To establish their permissiveness to infection, nasal ALI cultures were inoculated at the apical surface with a clinical SARS-CoV-2 isolate (BetaCoV/England/2/20) at an approximate multiplicity of infection (MOI) 0.1 - consistent with other studies (0.1-0.5)[12-14] - and monitored for infection over the next 72 h. Expression of SARS-CoV-2 *nucleocapsid (N)* gene and spike

129   (S) protein increased significantly over time, indicative of viral replication (Fig. 1E-F). This was

130   accompanied by the release of infectious viral particles, as determined by plaque assay of apical

131   washes on vero E6 cells, confirming productive infection (Fig. 1G). SARS-CoV-2 replication was

132   accompanied by a progressive decline in epithelial barrier integrity starting from 48 hours post-

133   infection (hpi), reflecting virus-induced epithelial dysfunction and/or potential cytopathic effect (Fig.

134   1H). These data established the suitability of the human nasal ALI system for modelling SARS-CoV-2
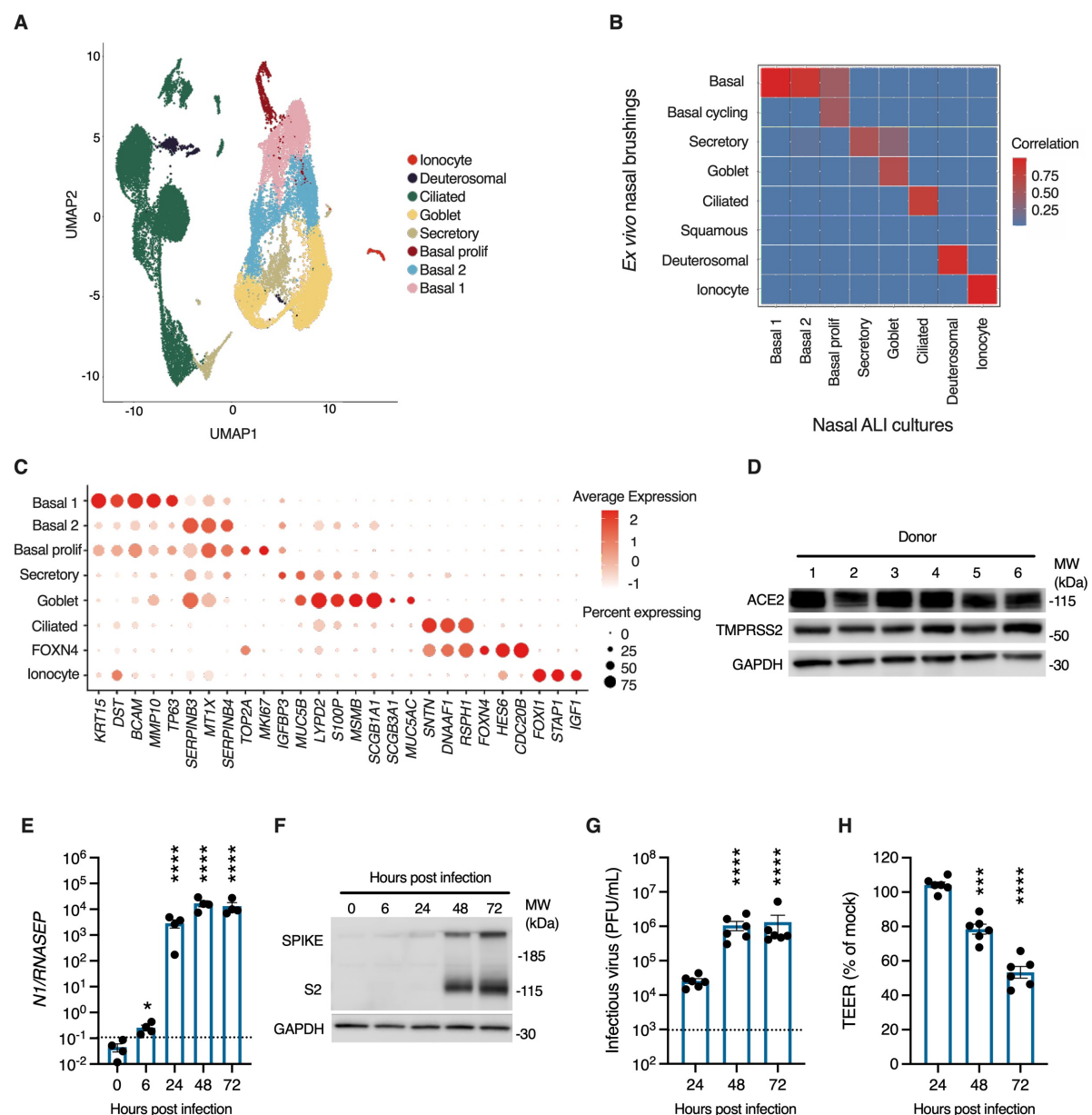
135   infection.

136

137

Figure 1. **Robust SARS-CoV-2 infection in a primary differentiated nasal epithelial ALI culture model.**

(A) UMAP visualisation of scRNA-seq data from nasal ALI cultures (28,346 single-cell transcriptomes from two representative donors) revealed six major cell types. (B) Correlation between the annotation from an external dataset of nasopharyngeal swabs and the assigned annotation of our scRNA-seq from nasal ALI culture following label transfer. (C) Dot plot demonstrating expression of key markers distinguishing cell types in annotated clusters, with intensity demonstrated by colour and size of the dot representing the proportion of cells expressing the marker. (D) Immunoblot demonstrating ACE2 and TMPRSS2 expression by donor, representative of n=3 experiments. Nasal ALI cultures were infected with SARS-CoV-2 (MOI 0.1) and subjected to various modalities to analyse infection. Whole-cell lysates were prepared at the indicated times for RT-PCR analysis of expression of (E) SARS-CoV-2 nucleocapsid (*N*) gene expression normalised to the housekeeper *RNASEP2* (average of n=2 repeat experiments in n=4 donors, mean $\pm$ SEM; * P < 0.05, **** P < 0.0001, ANOVA with Dunnett's post-test correction compared to 0h). (F) Whole-cell lysates were prepared at the indicated times for immunoblot analysis of expression of SARS-CoV-2 spike (S) and cleaved S2 protein expression (representative of repeat experiments in n=4 donors). (G) Release of infectious viral particles was determined by plaque assay of apical washings on permissive vero E6 cells (average of repeat experiments in n=6 donors, mean $\pm$ SEM; **** P < 0.0001, ANOVA with Dunnett's post-test correction compared to 24h). Dotted line represents lower limit of detection. (H) Transepithelial resistance (TEER) measurements upon infection (expressed as % of mock-infected wells, n=6 donors, mean $\pm$ SEM; *** P < 0.001, **** P < 0.0001, ANOVA with Dunnett's post-test correction compared to 24h).

Evidence of broad cellular tropism of SARS-CoV-2

To revisit the question of whether individual cell types are more or less permissive to SARS-CoV-2[13,14], we first examined viral gene expression by scRNA-seq analysis at 24 hpi, selected to represent an early stage in the progress of infection. While all cell types expressed viral transcripts, there were notable

164 differences both in the proportion of cells infected, and the relative abundance of different viral

165 transcripts within these cells (Fig. 2A). Based on differential gene expression analysis between cell

166 types (Wilcoxon rank sum test, one vs rest, P < 0.05), secretory and ciliated cells expressed higher

167 levels of viral transcripts than other cell types, with viral transcripts most abundant in secretory cells

168 (Fig. 2A, supplementary dataset 2). Deuterosomal cells also expressed abundant viral transcripts but

169 were a rare population within these cultures, possibly limiting the power of this analysis. Basal cells

170 are also located away from the apical surface; physical inaccessibility to apically-applied virus at this

171 time point might at least partially account for this observation. To investigate tropism further, we

172 undertook immunofluorescence analysis of viral spike (S) protein expression at 48 hpi (Fig. 2C-D, see

173 Fig. S4 for background spike immunoreactivity in uninfected cells). This analysis revealed broadly

174 similar proportions of ciliated, secretory and basal cells expressing S protein, with significantly lower

175 spike immunoreactivity in MUC5AC positive (goblet) cells (Fig. 2D). However, the mean pixel intensity

176 of S protein was significantly greater in ciliated cells than in other cell types, and significantly increased

177 in secretory cells compared to basal cells (Fig. 2D). To corroborate these findings, we undertook

178 analysis of intracellular virion-like structures (VLSs) at 48 hpi by transmission electron microscopy

179 (TEM, Fig 2E), focusing on ciliated and secretory/goblet cells (the latter cell types were grouped for

180 analysis as they could not be reliably distinguished based on morphology). Intracellular VLSs were

181 observed in both ciliated and secretory/goblet cells, predominantly towards the apical surface (Fig.

182 2E). Consistent with immunofluorescence analysis of S protein intensity, there was a significant

183 increase in the number of VLSs per cell in ciliated compared with secretory/goblet cells (Fig. 2E).

184 Collectively, these data suggested that the virus is capable of entering, and replicating in, all major

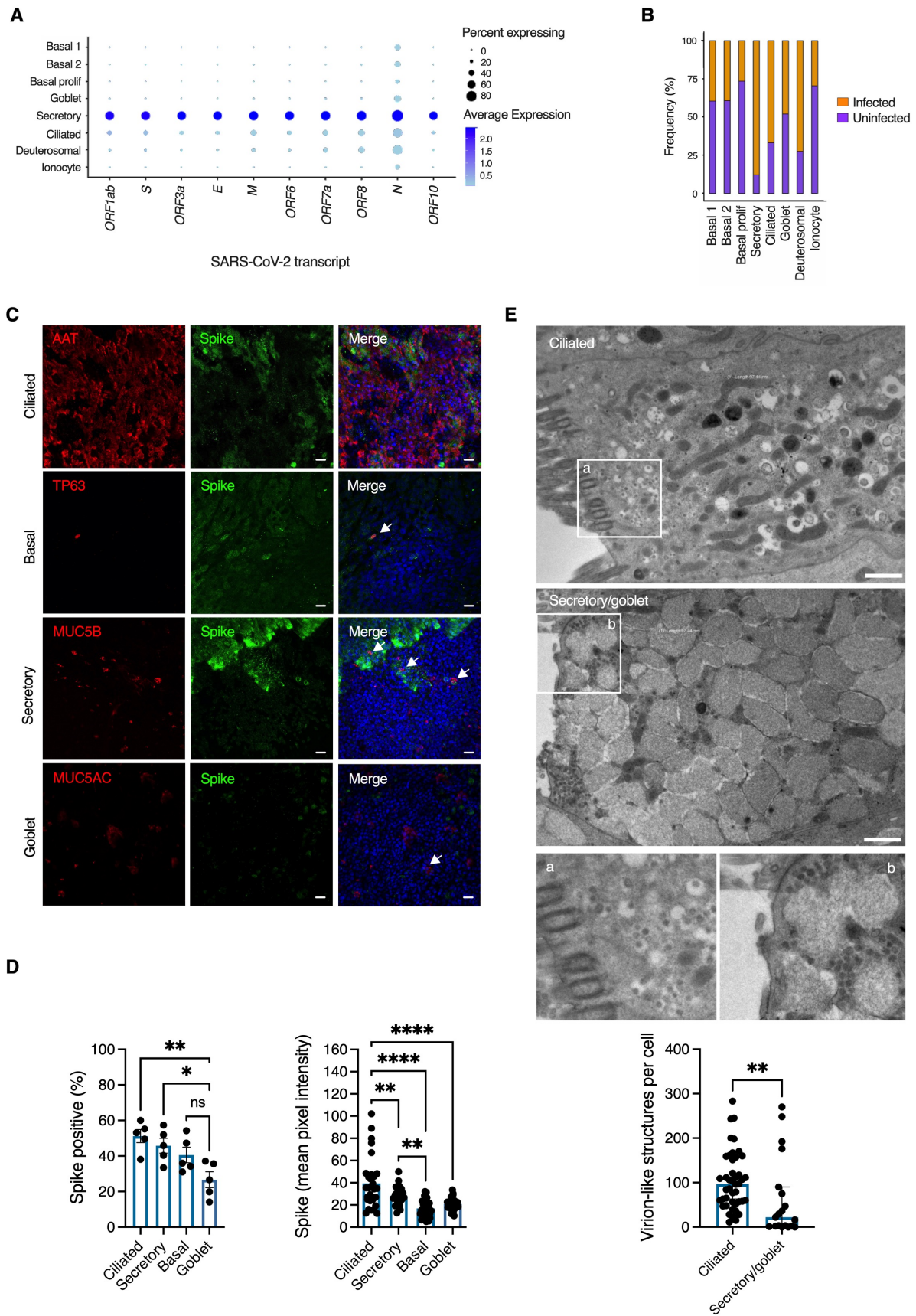185 nasal cell types, but with quantitative differences in efficiency.

186

188 **Figure 2. Broad tropism of SARS-CoV-2 for nasal cells**. Nasal ALI cultures were infected with SARS-

189 CoV-2 (MOI 0.1) and analysed using different modalities to explore tropism. At 24 hours post-infection

190 (hpi), cell suspensions were prepared from two representative donors for single-cell RNA sequencing

191 (scRNA-seq) and 28,346 individual transcriptomes passing QC were analysed. (A) Dot plot of scRNA-

192 seq data showing magnitude (colour) and proportion (size) of cell types expressing viral transcripts. E

193 = envelope; M = matrix; N = nucleocapsid; S = spike. (B) Relative proportion of infected cell types based

194 on expression of any viral transcript. Separately, nasal ALI cultures were fixed at 48 hpi and subjected

195 to immunofluorescence analysis. (C) Expression of viral S protein expression in ciliated (AAT), basal

196 cells (TP63), secretory (MUC5B) and goblet (MUC5AC) cells (arrowed) shown in (C). Scale bars = 10 μm

197 (representative of experiments in n=5 donors). (D) Quantification of cell-type specific expression of

198 viral S protein and S protein intensity at 48 hpi (n=5 donors, mean ± SEM; * P < 0.05, ** P < 0.01, ***

199 P < 0.001, **** P < 0.0001, ns = non-significant, ANOVA with Sidak's post-test correction for multiple

200 comparisons, indicated by lines). (E) Nasal ALI cultures were infected as above, fixed at 48 hpi for

201 transmission electron micrograph (TEM) analysis of SARS-CoV-2 infected ciliated and secretory/goblet

202 cells. Inserts (a) and (b) display virion-like structures in ciliated and secretory/goblet cells respectively.

203 Scale bars = 1 μm. Image analysis was undertaken to quantify virion-like structures as displayed in the

204 bar plot (n=3 donors, mean ± SEM ** P = 0.003, Mann-Whitney test).

205

206

207 **Characterisation of individual nasal cell responses to SARS-CoV-2**

208 Published *ex vivo* single-cell transcriptomic analyses report that nasal cell types exhibit the basal

209 expression of an innate antiviral gene signature, in the absence of viral infection, characterised by

210 several IFN-stimulated genes (ISGs)[10,11]. This signature correlated with *ACE2* expression, suggesting

211 conditioned expression to reduce susceptibility. Based on these reports, we examined scRNA-seq data

212 to characterise the innate antiviral response of nasal cells to SARS-CoV-2 infection at 24 hpi. In

213 unexposed cells, ISG signature scores were generated using context-specific ISGs from a published

214   IFN-treated nasal cell dataset[11] and compared using the Wilcoxon rank sum test. Gene set scores

215   greater than zero suggested expression levels higher than background gene expression, and was the

216   case for basal 1, secretory, goblet cells and ionocytes (Fig. 3A). The basal ISG signature was highest in

217   secretory cells despite abundant expression of viral RNA in these cells upon exposure to SARS-CoV-2

218   (Fig. 2A-B), suggesting basal ISG expression may not be sufficient to protect against infection. Next we

219   distinguished cells in three experimental conditions: unexposed (mock-infected); SARS-CoV-2-

220   exposed but uninfected (these 'bystander' cells would theoretically be exposed to IFNs and other

221   paracrine signals, but not infected); and SARS-CoV-2-infected (as defined by detectable expression of

222   SARS-CoV-2 transcripts). We undertook differential expression (DE) analysis between mock and

223   bystander or infected cells, labelling ISGs derived from the same list of context-specific ISGs (Fig. 3B,

224   supplementary datasets S3-4). There was minimal transcriptional response to infection in bystander

225   cells, including the absence of ISG induction, suggesting a lack of substantial paracrine IFN signalling

226   at this timepoint in keeping with reports in other airway models[25,27,28]. Interestingly, *IFITM* genes (ISGs

227   which have been paradoxically implicated in SARS-CoV-2 entry[33]) were downregulated in some

228   bystander cell populations. There was also minimal evidence of ISG induction in SARS-CoV-2 infected

229   cells, especially secretory, deuterosomal and goblet cells (Fig. 3B). In secretory and ciliated several

230   ISGs relating to antigen processing or presentation were downregulated upon infection (Fig. 3B). Basal

231   cells expressed a modest number of ISGs upon infection, specifically genes of the *IFITM* family, *IFI27*

232   and *IFI6* and the negative regulator of IFN-I signalling, *ISG15.* Consistent with this finding, gene-set

233   enrichment analysis (GSEA) revealed upregulation of IFN alpha/gamma responses in infected basal

234   cell populations but not in other cell types (Fig. 3C). The transcriptional response of infected secretory

235   and ciliated cells was characterised by widespread downregulation of expression, which may reflect

236   viral co-optation of transcriptional machinery of host cells, but this effect was not uniform. In

237   agreement with previous reports[34,35], genes related to oxidative phosphorylation were prominent

238   amongst downregulated genes, as were antigen presentation pathways. Pathway analysis also

239   predicted upregulation of NF-KB signalling in basal, secretory, goblet and ciliated cells, consistent with

240   previous findings[27,36]. Using DoRoTHea to explore regulon activity in these populations revealed higher

241   predicted *NFKB2* activity but limited evidence of widespread activation of IFN-mediated signalling (Fig.

242   S5). Transcripts for IFN-I (*IFNB, IFNK, IFNA5)* and IFN-III (*IFNL1)* were not significantly differentially

243   expressed and were detectable in only a small minority (~ 0.4%) of infected secretory cells (Fig. S6).

244   Whilst potentially consistent with the lack of paracrine signalling at this timepoint, this might also

245   reflect transient expression and/or insensitivity of detection by scRNA-seq; a similar pattern was

246   observed for other cytokines and chemokines (Fig. S6). Overall, this analysis showed that despite

247   evidence of NF-KB activation at 24 hpi, there was a minimal IFN response to SARS-CoV-2 in the cell

248   types with the highest levels of infection, consistent with previous reports in non-nasal epithelial
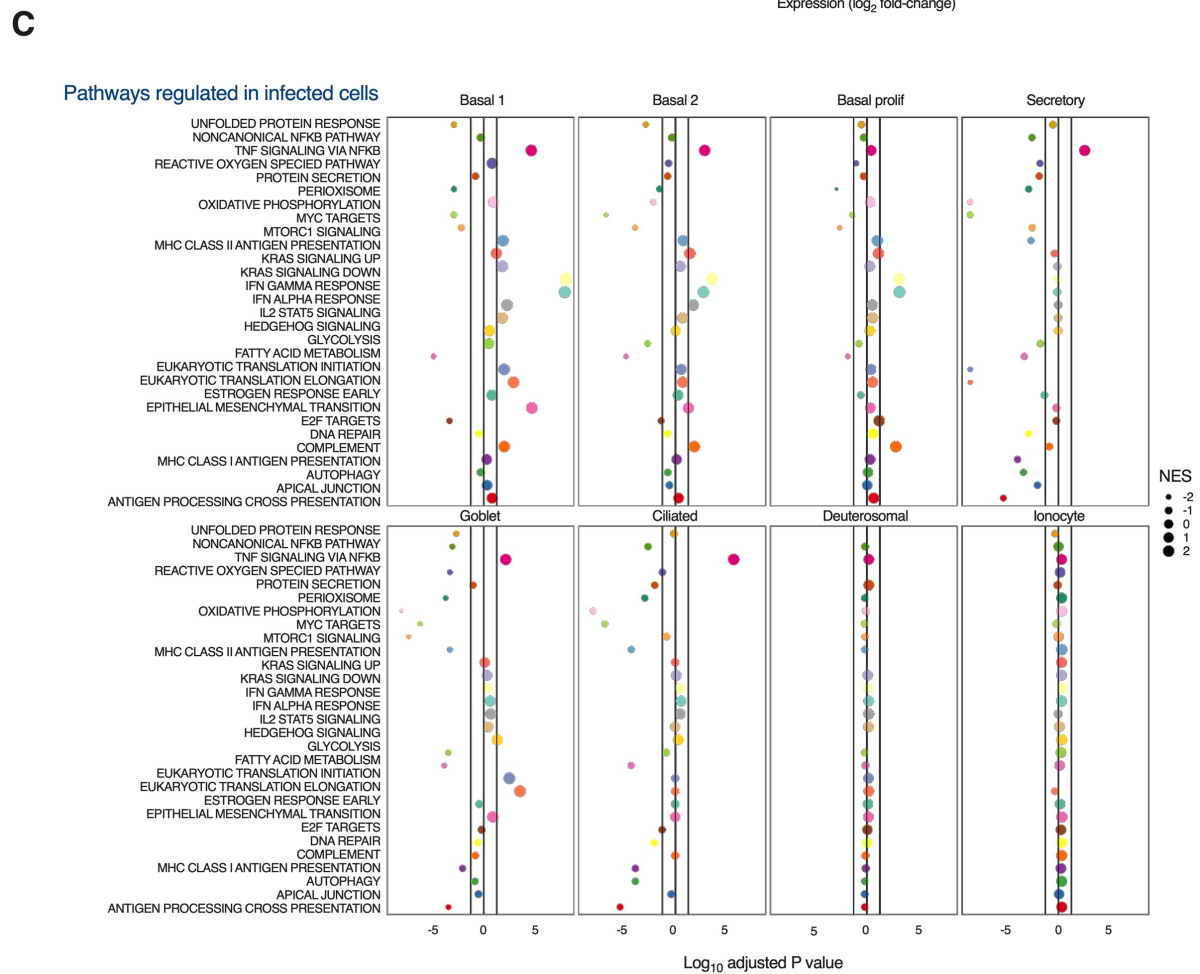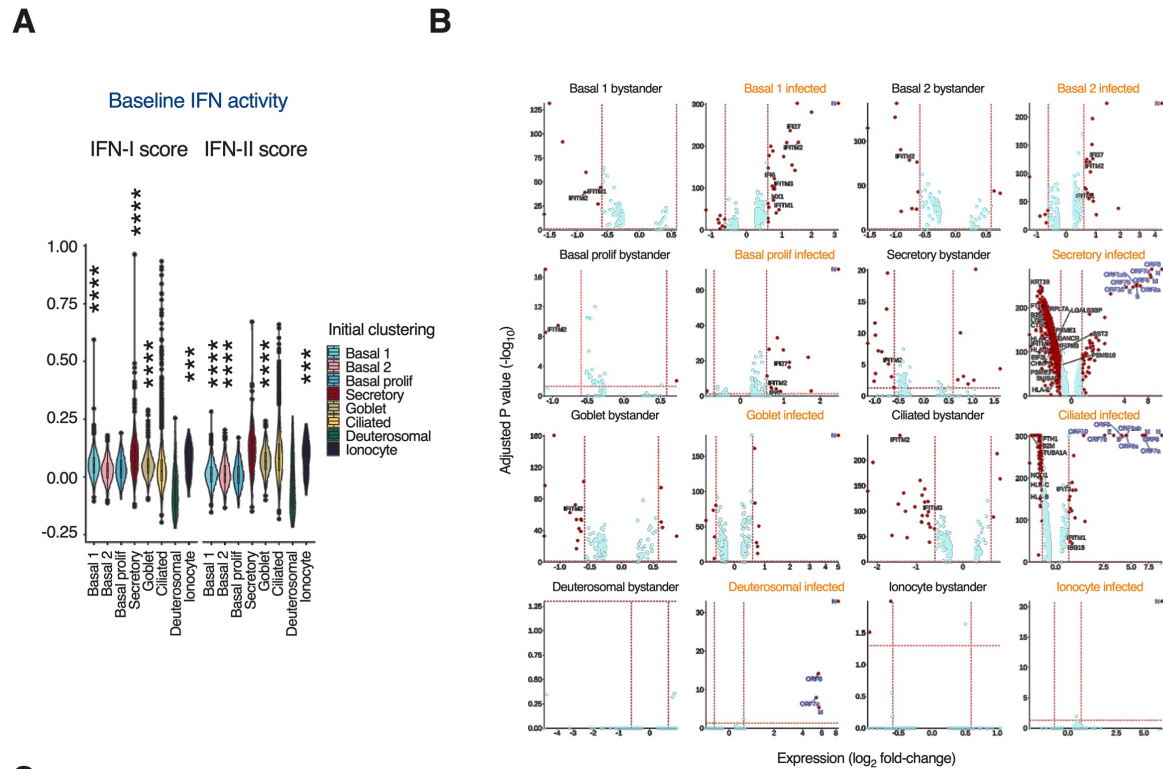
249   cells[25,27,28].

250

251

252 **Figure 3. Characterisation of individual nasal cell transcriptional responses to SARS-CoV-2.** Nasal ALI

253 cultures were infected with SARS-CoV-2 (MOI 0.1). At 24 hours post-infection (hpi), cell suspensions

254 were prepared from two representative donors for single-cell RNA sequencing (scRNA-seq) and

255 28,346 individual transcriptomes passing QC were analysed. (A) A composite interferon-stimulated

256 gene (ISG) signature score was defined based on a published nasal cell dataset from cells treated with

257 IFN alpha and IFN gamma. Gene set scores greater than zero suggest expression levels higher than

258 background gene expression. Wilcoxon rank sum testing was performed for each cell type vs all with

259 Benjamini-Hochberg correction (* $P < 0.05$, ** $P < 0.01$, *** $P < 0.001$ **** $P < 0.0001$). (B) Differential

260 expression (DE) analysis by Wilcoxon rank sum test was undertaken to compare mock-infected cell

261 transcriptomes with those from bystander cells (without detectable viral transcripts) and infected cells

262 (with detectable viral transcripts) from the virus-exposed cultures. Volcano plots were generated with

263 vertical lines marking -/+ 1.5 fold change cut-offs (note log_2 scale) and the horizontal line marking an

264 adjusted P value cut-off of 0.05 (< 0.05 was considered statistically significant). Individual genes

265 coloured as non-significant (light blue) and significant (red). Labels indicate viral transcripts (dark blue)

266 and epithelial-cell specific ISGs (black). (C) Gene-set enrichment analysis was undertaken by ordering

267 genes by fold change difference between mock-infected and infected cells by cluster. Vertical lines

268 indicated adjusted P value cut-off of 0.05. NES = normalised enrichment score.

269

270

271 **Kinetics of innate IFN-I/IFN-IIIs response to SARS-CoV-2**

272 To investigate the kinetics of the IFN-I/III response, expression of IFN-I (*IFNA1* and *IFNB*) and IFN-III

273 (*IFNL1*) was examined by RT-PCR at 6, 24, 48 and 72 hpi at the same MOI (0.1) as previous experiments.

274 Induction of *IFNL1* and *IFNB* was low at 24 hpi, consistent with scRNA-seq findings, but increased

275 significantly by 48 and 72 hpi (Fig. 4A). *IFNA1* was not induced, as observed in our scRNA-seq data.

276 Compared to the timing of initiation of viral gene expression - which was detectable at 6 hpi and

277 approached its maximum level by 24 hpi (Fig. 1E) - the induction of IFNs appeared delayed, as

278   suggested by previous studies[12,14,36]. Infection was accompanied by progressive upregulation of

279   proinflammatory cytokines such as *IL6, IL1B* and *TNF*, consistent with initiation of an NF-KB-dependent

280   inflammatory response (Fig. 4B). To look for evidence of a paracrine response to IFN-I/III, we analysed

281   expression of the ISGs *RSAD2* and *USP18* by RT-PCR, as well as the expression of RSAD2, USP18, ISG15

282   and MX1 proteins by immunoblotting. There was an increase in ISG mRNA and protein expression at

283   later times following the onset of *IFN* gene expression (Fig. 4C-D), potentially suggestive of paracrine

284   JAK-STAT signalling. To explore early induction of IFNs in more detail, we compared the response to

285   SARS-CoV-2 with other RNA respiratory viruses, influenza A virus (IAV) and parainfluenza virus 3

286   (PIV3). In this experiment, significant induction of *IFNB* and *IFNL1* occurred in response to both PIV3

287   and IAV, but not SARS-CoV-2, at 24 hpi (Fig. S7), and was accompanied by upregulation of ISGs *USP18*

288   and *RSAD2*. Infection of cell lines at high MOI are reported to enhance the relatively inefficient IFN-I

289   induction to SARS-CoV-2[25]. To confirm that the attenuated production of *IFNL1* and *IFNB* at early times

290   was not dependent on MOI, we repeated SARS-CoV-2 infections at 20-fold higher MOI (2), alongside

291   IAV (Fig. 4E), or a preparation of Sendai virus (SeV) containing a high proportion of immunostimulatory

292   defective viral genomes[32] as a positive control (Fig. S8). At 6 hpi, a time point at which *IFNB* and *IFNL1*

293   were significantly induced by IAV, there was no detectable response to SARS-CoV-2 (Fig. 4E).

294   Compatible observations were made with SeV (Fig. S8). At 24 hpi, SARS-CoV-2 exposure led to no

295   detectable induction of *IFNB* and significantly less *IFNL1* than IAV (Fig. 4E). This differential response

296   was reflected in the robust expression of ISGs *RSAD2, USP18* and *ISG15* at 24 h post-inoculation with

297   IAV but not SARS-CoV-2 (Fig. 4F). These observations recapitulated our previous RT-PCR and scRNA-

298   seq data with a lower MOI, and are consistent with other reports[12,27,37]. Collectively, the results

299   indicate that nasal epithelial cells express IFN-I/IIIs during SARS-CoV-2 infection, but that the response

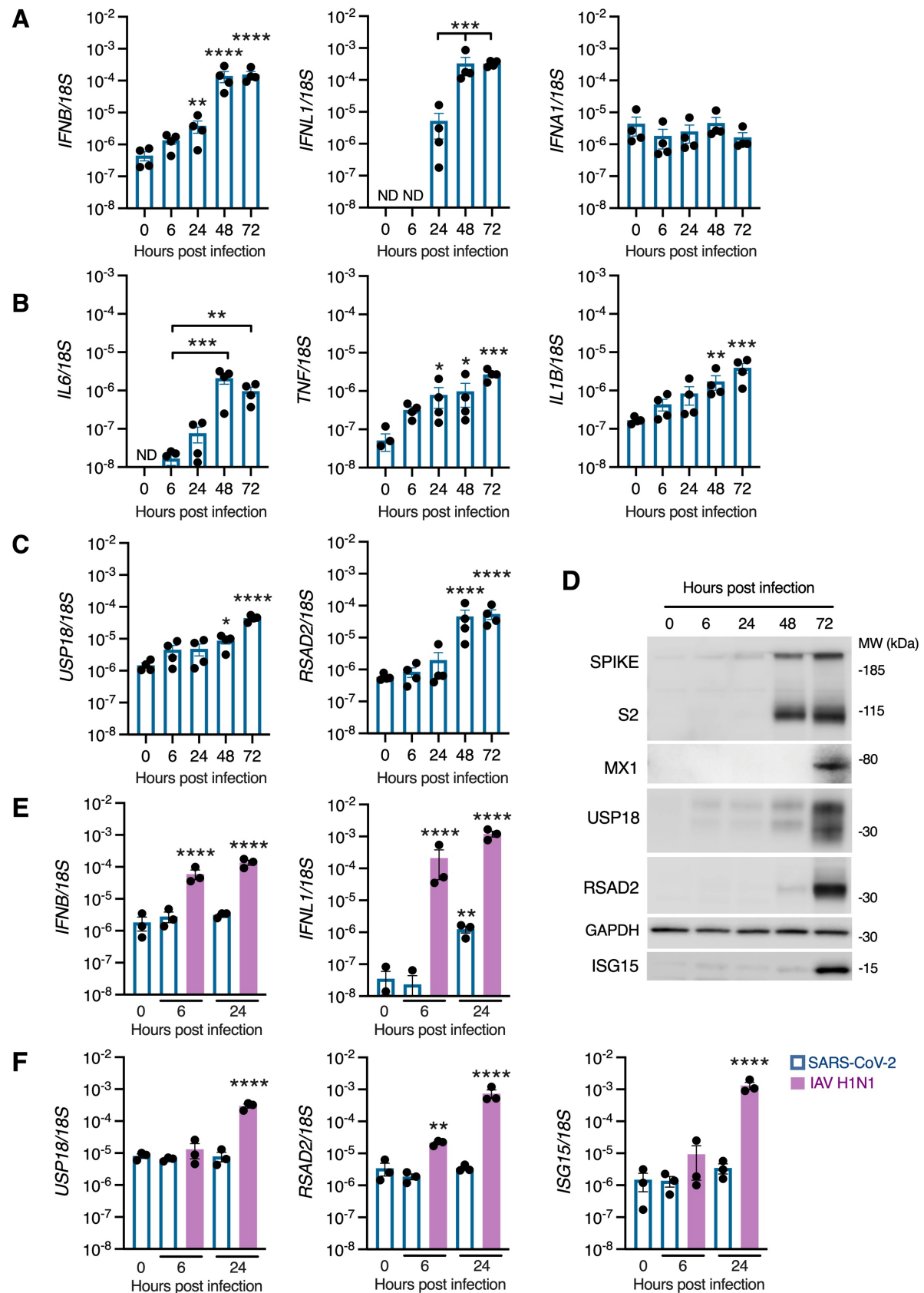300   is delayed relative to viral replication.

301

Figure 4. Delayed induction of IFN-I/III signalling in SARS-CoV-2-infected nasal ALI cultures. Nasal ALI

cultures were infected with SARS-CoV-2 (MOI 0.1). Whole-cell lysates were prepared at the indicated

305 times for RT-PCR analysis of expression of (A) *IFNB*, *IFNL1* and *IFNA1* (B) *IL6*, *TNF* and *IL1B* and (C)

306 *USP18* and *RSAD2* (average of n=2 repeat experiments in n=4 donors, mean ± SEM; * P < 0.05, ** P <

307 0.01, *** P < 0.001 **** P < 0.0001, ANOVA with Dunnett's post-test correction compared to 6h [B,

308 *IL6*], 24h [A, *IFNL1*] or 0h [all others]). ND, Not detected. (D) Whole-cell lysates were prepared at the

309 indicated times for immunoblot analysis of S/S2, MX1, USP18, RSAD2 and ISG15 expression

310 (representative of experiments in n=4 donors). Nasal ALI cultures were infected with SARS-CoV-2 or

311 influenza A virus (IAV H1N1, purple bars) at MOI 2. Whole-cell lysates were prepared at the indicated

312 times for RT-PCR analysis of expression of (E) *IFNB*, *IFNL1* and (F) the ISGs *USP18*, *RSAD2* and *ISG15*

313 (n=3 donors, mean ± SEM; * P < 0.05, ** P < 0.01, *** P < 0.001 **** P < 0.0001, ANOVA with Dunnett's

314 post-test correction compared to 0h).

315

316

317 **IFN-signalling dominates the nasal host response to SARS-CoV-2 at the protein level**

318 To validate and extend these findings, we undertook an unbiased assessment of the host response to

319 SARS-CoV-2 infection by proteomics analysis. Whole-cell lysates were prepared from SARS-CoV-2 and

320 mock-infected nasal ALI cultures from six donors at 72 hpi. Lysates were analysed by quantitative mass

321 spectrometry (quality control data in Fig. S9). Overall, this analysis detected the differential expression

322 (DE) of 180 proteins including viral proteins such as S, M, N, ORF1AB, ORF3A and ORF8 (Fig. 5A

323 supplementary dataset S4). The most highly increased host protein was Sorting Nexin 33 (SNX33), an

324 endosomal protein that has not yet been implicated in the life cycle of SARS-CoV-2. Notably, other

325 SNX proteins (e.g. SNX17 and SNX2) are involved in viral trafficking[38,39]. Infected and uninfected cells

326 clustered together by principal component analysis (Fig. 5B). Inspection of the DE proteins confirmed

327 a robust host innate immune response, dominated by ISG products (Fig. 5A). Functional annotation

328 revealed an enrichment of antiviral response and especially IFN-I signalling pathways (Fig. 5C, Table

329 S2). These data are consistent with our earlier findings and contrary to prior reports in cell lines or

330 human bronchial/tracheal epithelial cultures, where a robust endogenous IFN-I/III response to SARS-

331   CoV-2 was not detected[26-28]. Key antiviral ISG proteins identified included IFIT1-3, MX1-2, and the OAS

332   cluster (OAS1-3), the latter associated with genetic susceptibility to severe COVID-19[19] (Fig. 5C).

333   Significantly downregulated pathways were also identified, including TRIF-dependent toll-like

334   receptor signalling, as well as RNA polymerase II transcription and endosomal transport (Table S3).

335   This implied viral subversion of critical host functions, including host gene transcription, protein

336   trafficking and viral sensing. Proteins involved in the maintenance of epithelial tight junctions were

337   also downregulated, consistent with the loss of barrier integrity observed in earlier experiments (Fig.
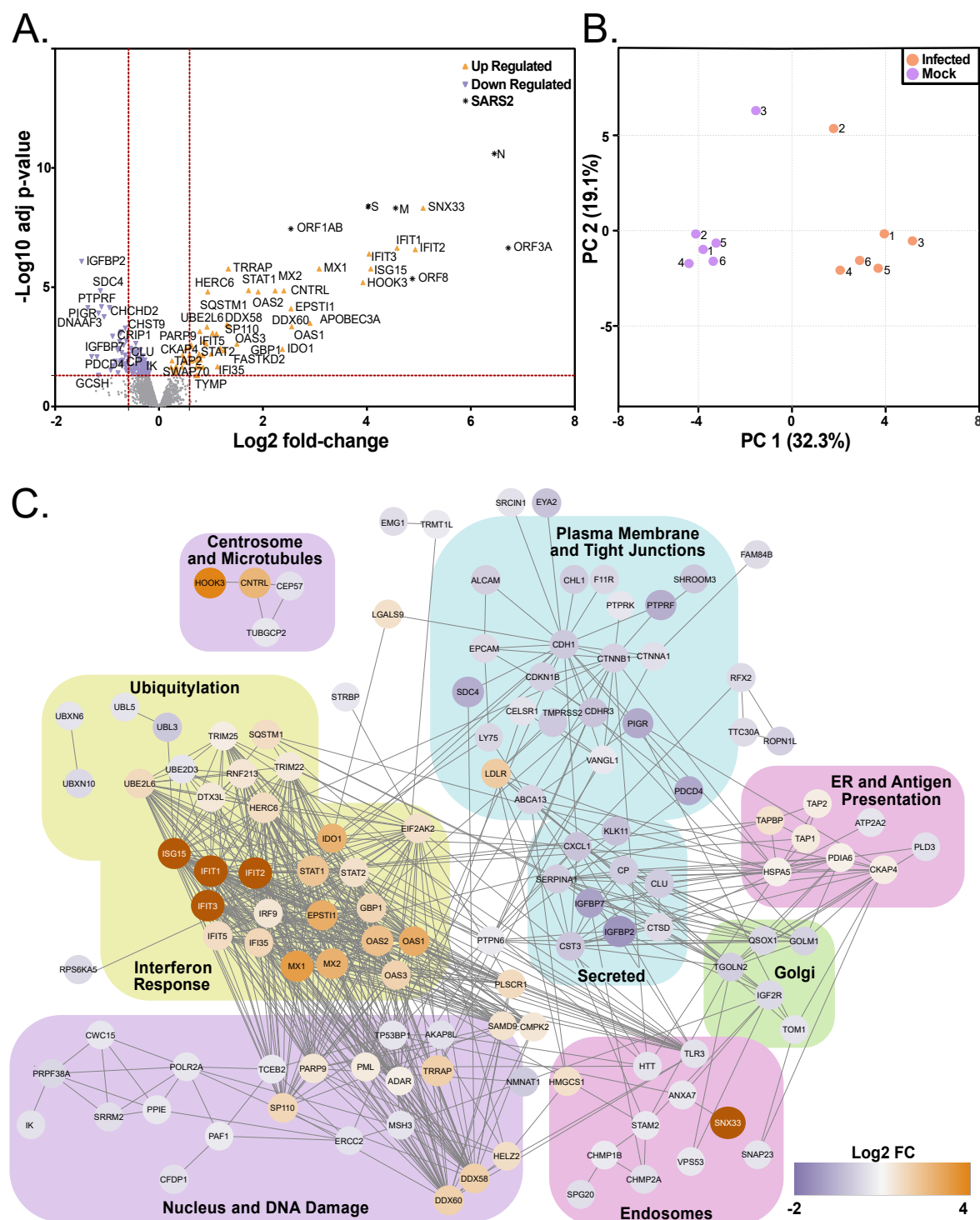
338   1H).

339

Figure 5. An ISG response dominates the proteome of SARS-CoV-2 infected nasal ALI cultures.

Differential proteomic profiling of SARS-CoV-2-infected nasal ALI cultures. Mass spectrometry-based proteomics was carried out on whole-cell lysates prepared at 72 hpi (n=6 donors per condition). (A) Volcano plot illustrating 180 differentially expressed proteins with increased (orange points) and decreased (purple points) expression in infected as compared to mock-infected samples. Dotted red

346   lines indicate those proteins with a fold change of > 1.5 and adjusted p values <0.05. (B) Principal

347   component analysis of the whole proteome data set. (C) Functional annotation network of

348   differentially expressed proteins.

349

350

351   **Antiviral activity of IFN-I/III towards SARS-CoV-2 infection**

352   Given the prominence of the IFN-I/III response in the proteome of SARS-CoV-2-infected cells at later

353   times post-infection, a key question was whether this IFN-I/III response had any impact on SARS-CoV-

354   2 replication. To address this question, nasal ALI cultures were treated with the JAK inhibitor

355   ruxolitinib (RUX). RUX antagonises signalling downstream of IFNAR and IFNLR, owing to the

356   involvement of JAK1 in both signalling pathways. We reasoned that blocking paracrine IFN-I/III

357   signalling would reveal its impact, if any, on SARS-CoV-2 replication. Cells were treated with 10 µM

358   RUX (a dose optimised in prior experiments[40]) or vehicle control (DMSO) in the basal medium for 24

359   hours prior to infection. Nasal cultures were infected at the apical surface (MOI 0.1), inhibitors were

360   refreshed every 24h and infection was monitored up to 96 hpi. Lysates were prepared and analysed

361   by RT-PCR and immunoblot. RUX treatment abolished expression of ISGs *USP18, RSAD2 and ISG15* at

362   the mRNA and protein level (Fig. 6A-B), indicating that ISG induction was dependent on paracrine IFN-

363   I/III signalling, as previously suggested (Fig. 4D). By 96 hpi, approximately 24 hours after ISGs were

364   reliably detected at the protein level (Fig. 4D, Fig. 5A-C), blockade of this endogenous IFN response by

365   RUX led to a significant increase in both viral gene expression, assessed by RT-PCR (*N* gene) and

366   immunoblot (S/S2 protein, Figs 6B-D), and apical release of infectious virus measured by plaque assay

367   (Fig. 6E). These data provided further evidence that SARS-CoV-2 triggered an endogenous paracrine

368   IFN-I/III response in nasal cells, which once established began to impact SARS-CoV-2 replication.

369   An important follow-up question was whether nasal cells could mount an antiviral state to SARS-CoV-

370   2, providing IFN-I/III was delivered in a timely fashion. To address this, nasal ALI cultures were pre-

371   treated with exogenous IFNβ (1000 IU/mL) or IFNλ1 (100 ng/mL) for 16h to induce an antiviral state,

372   subsequently infected with SARS-CoV-2 at MOI 0.01 and examined at 48 hpi. Analysis of infection by

373   immunoblotting of whole-cell lysates for spike (S/S2) protein expression or plaque assay of apical

374   washes demonstrated a significant reduction in infection with either IFNβ or IFNλ1 pre-treatment (Fig.

375   7A-B). This was accompanied by robust induction of antiviral ISG products (Fig. 7A), and preservation

376   of barrier integrity (Fig. S10). It is worth noting that the ISG expression induced in response to

377   recombinant IFN-I/III at 48 hpi was substantially greater than that induced by endogenous IFN-I/III

378   production (Fig. 7A). Thus exogenous IFN-I/III was capable of inducing in the nasal epithelium an

379   antiviral state that potently inhibited SARS-CoV-2 infection, providing it was delivered (a) prior to

380   infection, and (b) at sufficient concentration. This IFN-sensitivity of SARS-CoV-2 contrasts with the

381   relative resistance of SARS-CoV[21]. These data suggest that mucosal delivery of IFNβ or IFNλ1 is a

382   potential therapeutic strategy for SARS-CoV-2. In clinical practice, IFNs are unlikely to be used prior to

383   infection, unless this is part of a prophylactic regimen. To determine the effectiveness of exogenously

384   applied IFNs once SARS-CoV-2 infection is underway, infected cells were treated with IFNβ or IFNλ1

385   at 6 or 24 hpi and examined for S/S2 protein expression by immunoblot (Fig. 7C-D) and release of

386   infectious virus by plaque assay (Fig. 7E). In this experiment, IFNβ and IFNλ1 treatment at 6 hpi

387   continued to impact on SARS-CoV-2 infection, whereas addition after 24 hpi had minimal effect.

388   Interestingly, ISG induction was still observed in response to IFN treatment at 24 hpi, albeit at reduced

389   magnitude in the case of IFNβ (Fig. 7C-D). These data suggest that SARS-CoV-2 may impair, but does

390   not abolish, JAK-STAT signalling in infected cells, implying that recombinant IFNs may have a

391   therapeutic role in established SARS-CoV-2 infection, as recently shown in animal models[9] and in early

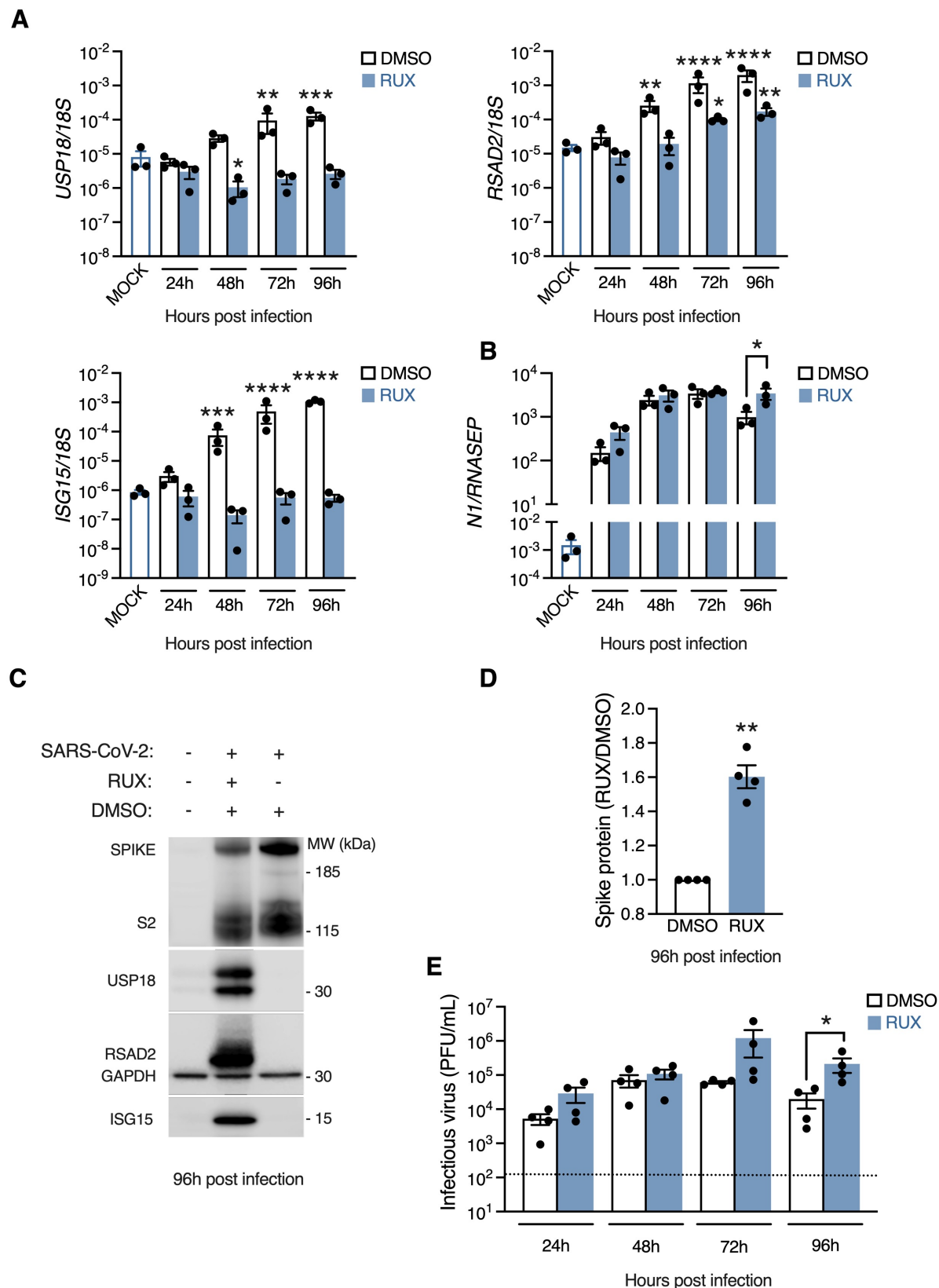392   phase clinical trials[41].

393

394

Figure 6. Impact of endogenous IFN-I/III signalling on SARS-CoV-2 infection. Nasal ALI cultures

treated with ruxolitinib (RUX, 10 μM) or DMSO vehicle for 24 h prior to infection (MOI 0.1). Whole-

397   cell lysates were prepared at the indicated times for RT-PCR analysis of expression of (A) the ISGs

398   *USP18, RSAD2* and *ISG15* (n=3 donors, mean ± SEM; *** P < 0.001, **** P < 0.0001, ANOVA with

399   Dunnett's post-test correction compared to mock-infected cells) or (B) viral *N* mRNA (n=3 donors,

400   mean ± SEM; * P = 0.035 ANOVA with Sidak's post-test correction compared to DMSO control). (C)

401   Whole-cell lysates were prepared at 96 hpi for immunoblot analysis of viral S/S2 protein and host

402   RSAD2, USP18 and ISG15 protein expression (representative blot shown of experiments in n=4

403   donors). (D) Densitometry analysis of S+S2 protein intensity relative to GAPDH, normalised to the

404   DMSO control (data from C, n=4 donors, mean ± SEM; ** P = 0.003, one-sample t test). (E) Plaque

405   assay of apical washes collected at the times indicated showing a significant increase in infectious

406   particle release at 96 hpi (same experimental conditions as C-D; n=4 donors, mean ± SEM; * P = 0.015,

407   ANOVA with Sidak's post-test correction compared to DMSO control). Dotted line indicates lower limit
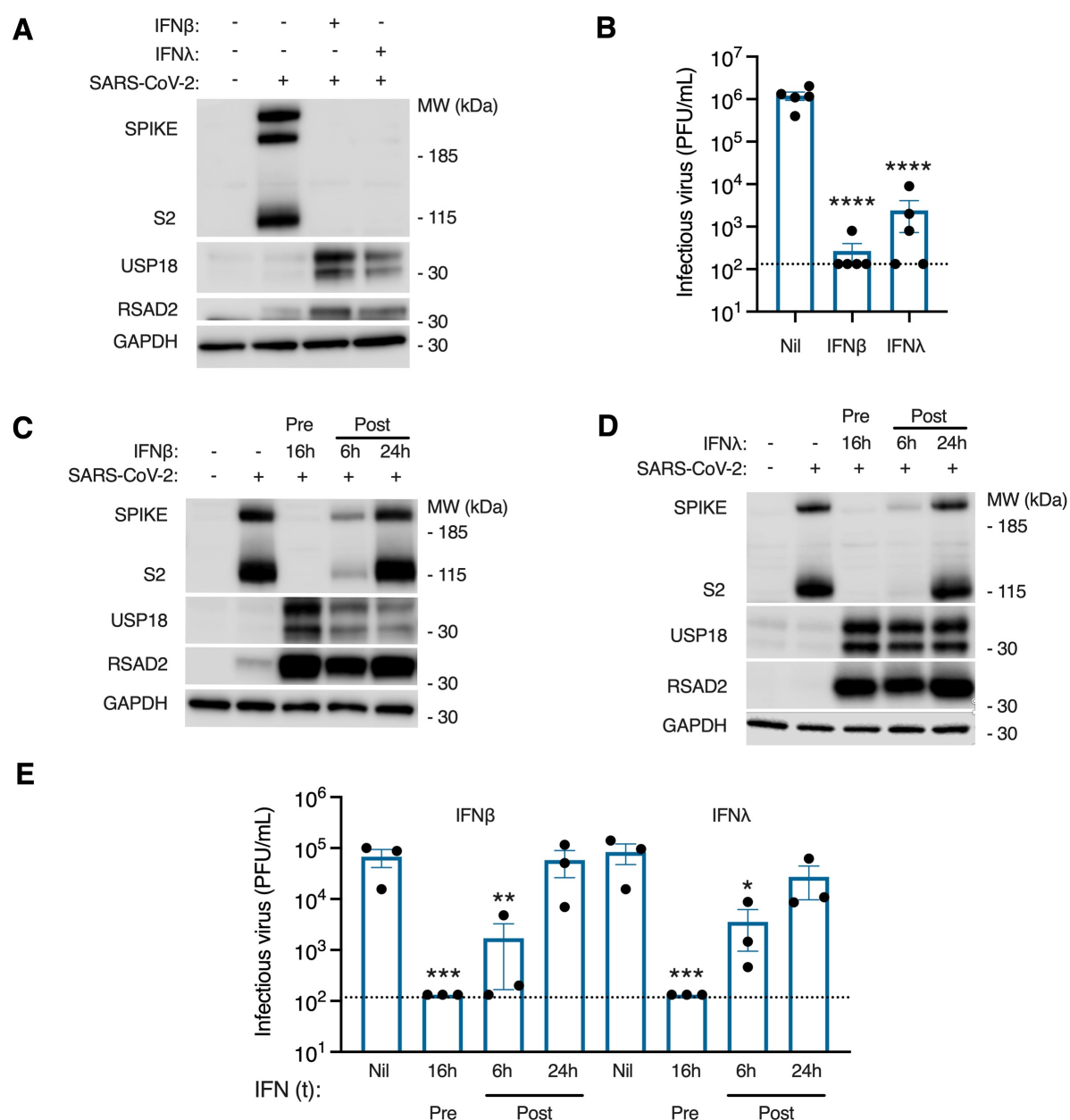
408   of assay detection.

409

Figure 7. Exogenous IFN-I/III treatment controls SARS-CoV-2 replication. Nasal ALI cultures were pre-treated for 16 h with IFNβ (1000 IU/mL) or IFNλ1 (100 ng/mL) prior to infection (MOI 0.01). (A) Immunoblot of whole-cell lysates prepared from nasal ALI cultures at 48 hpi (representative of experiments in n=4 donors). (B) Plaque assay of apical washes showing significant reduction in infectious particle release at 48 hpi if pre-treated with IFNβ (1000 IU/mL) or IFNλ1 (100 ng/mL) (same experimental conditions as A; n=5 donors, mean ± SEM; **** P < 0.0001, ANOVA with Dunnett's post-test correction compared to untreated control). (C-D) Immunoblot of whole-cell lysates prepared at 48 hpi. Nasal ALI cultures were either pre-treated with IFNβ (1000 IU/mL, C) or IFNλ1 (100 ng/mL, D)

419   for 16h prior to infection with SARS-CoV-2 or IFN treatment was applied at 6 or 24 hpi. Results

420   representative of experiments in n=3 donors. (E) Plaque assay on apical washes collected at 48 hpi

421   from experiments in C-D (n=3 donors, mean $\pm$ SEM; * P < 0.05, ** P < 0.01, *** P < 0.001, ANOVA with

422   Dunnett's post-test correction compared to untreated control). Dotted line indicates lower limit of

423   assay detection.

424

425 **DISCUSSION**

426 We report the most comprehensive characterisation of the human nasal epithelial response to

427 experimental SARS-CoV-2 infection to date, revealing a response dominated at later stages by IFN-

428 I/IIIs and their downstream ISG products. This response partially contained SARS-CoV-2 at later times

429 post-infection, while recombinant IFN-I/III treatment potently blocked SARS-CoV-2 replication,

430 suggesting that mucosal delivery of IFNs could be a promising strategy for post-exposure prophylaxis.

431 The nasal mucosa is likely to be a main point of entry of SARS-CoV-2. Prior single-cell transcriptomic

432 studies implied an abundance of target cells in the nasal mucosa and further suggested that they may

433 be poised to mount an antiviral response[10]. Yet few studies to date have characterised SARS-CoV-2

434 replication in primary human differentiated nasal cells[12-14], while we analyse the host-virus interaction

435 comprehensively, at single-cell resolution and utilising proteomics. Our findings indicate that the host

436 response to SARS-CoV-2 in nasal epithelium is dominated by paracrine IFN-I/III signalling, albeit this

437 response is kinetically delayed. These data contrast with initial reports that SARS-CoV-2 did not induce

438 a robust IFN response in airway epithelial cells[26-28], but are consistent with emerging evidence of IFN-

439 I/III induction in nasal swabs from patients with COVID-19[15,42-44] and with more recent findings in lung

440 airway models[36,43,45-47]. Blockade of the endogenous IFN response had an impact on SARS-CoV-2

441 infection at later stages post-infection, once the IFN response was established, underscoring the

442 delayed kinetic but also emphasising its functional relevance. While the impact of endogenous IFN-

443 I/III signalling upon SARS-CoV-2 replication has not to our knowledge been investigated in nasal cell

444 models, our data are consistent with recent findings in some[43,47], but not all epithelial model

445 systems[27,45]. Our experiments with IAV, PIV3 and SeV - viruses which induced the robust early

446 expression of IFN-I/III, in line with previous studies[12,27,37] - confirm that this delay was not due to an

447 intrinsic property of nasal epithelial cells. The expression of IFN evasion proteins[37,48], the sequestration

448 of viral replication machinery within cytosolic vesicles[49], as well as global reductions in host mRNA

449 content[50] and translational shutdown[51-53] induced by SARS-CoV-2 presumably underlie its capacity to

450 subvert early IFN induction in infected cells. Consistent with this, there was evidence of

451   downregulation of immune pathways including TLR signalling in the proteome of infected cells.

452   However, an important question is what molecular patterns are responsible for IFN-I/III induction at

453   later times. Recent evidence implicates MDA5 as a major sensor of SARS-CoV-2 RNA in epithelial

454   cells[45-47], while other findings suggest a contribution from virus-mediated damage occurring after

455   several days of infection[54]. It will be important to address the relative contribution of host damage-

456   associated molecular patterns versus viral pathogen-associated molecular patterns (e.g. defective

457   viral genomes) accumulating during replication.

458   IFN-I/III signalling is plausibly implicated in protection against life-threatening COVID-19[18-20].

459   Consistent with this, circulating immune cells of patients with severe COVID-19 exhibit impaired ISG

460   responses[55-57]. However, whether the local airway IFN response in the early stages of infection has a

461   decisive role in shaping the subsequent clinical outcome of COVID-19 remains to be conclusively

462   determined. A compelling recent scRNA-seq study reported that patients going on to develop severe

463   disease exhibited a muted ISG response in the nasal airway, in contrast to those with milder disease[15],

464   and is supported by independent findings of attenuated nasal ISG induction in patients with

465   autoantibodies to IFN-I[58], who are prone to more severe disease[20]. Additional strands of evidence

466   suggest a potential link between airway IFN-I/III competence and clinical outcome in COVID-19. Age

467   remains the strongest risk factor for poor outcome in COVID-19, and the efficiency of IFN-I/III

468   induction is known to decline with advancing age[59], and appears to be greater in the nasal airways of

469   children than adults infected with SARS-CoV-2[60]. Other relevant environmental influences, such as

470   exposure to cigarette smoke or other viral infections, are also reported to perturb IFN-I/III responses

471   of airway cells in ways that may be relevant to COVID-19 pathogenesis[43,61].

472   The main limitation of our data in this nasal epithelial culture system is that it did not account for

473   professional immune cells present in the nasal mucosa, for example plasmacytoid dendritic cells[62],

474   which are capable of more rapidly mounting an IFN-I/III response to SARS-CoV-2[63], potentially tipping

475   the scales in favour of the host[64]. We studied cells derived from adult donors, however it is possible

476   that nasal cells from paediatric donors, who are naturally less susceptible to severe COVID-19, may

477   behave differently in terms of their reduced permissiveness to SARS-CoV-2 and/or the greater

478   efficiency of their innate IFN response[60,65]. Furthermore, SARS-CoV-2 variants with mutations in the

479   spike gene have emerged worldwide whilst we were undertaking the experiments described here;

480   these variants may impact viral replication and/or host immunity, and should be included in future

481   studies.

482   Nevertheless, our data, employing a variety of complementary methods, indicate that SARS-CoV-2 has

483   a relatively broad tropism for nasal epithelial cells, confirming suggestions from prior scRNA-seq

484   studies[8,10], other *in vitro* studies of primary nasal[14] and tracheobronchial cells[24,36], and importantly

485   recent scRNA-seq studies of nasal samples from COVID-19 patients[15]. We also identify tropism for the

486   rare deuterosomal cell, marked by expression of FOXN4, as recently reported[36,61,66]. Our findings

487   contrast with the results of Hou and colleagues, who reported exclusive tropism of SARS-CoV-2 for

488   ciliated cells in the nasal airway[13]. It is not immediately clear how to reconcile these findings, given

489   that secretory cells express relevant entry receptors[10,13] and have been identified as a major infected

490   cell type in infected patients[66]. Hou and colleagues used a fluorescent reporter virus, the tropism of

491   which might have been slightly narrower than clinical isolates. It is also worth noting that while we

492   show that all cell types contained SARS-CoV-2 protein, there was a significant reduction in the

493   proportion of goblet cells expressing spike protein, and the intensity of spike immunodetection was

494   significantly greater in ciliated and secretory cells than basal or goblet cells. Ciliated cells also

495   contained more virion-like structures per cell. Collectively, this implies that although all cell types are

496   permissive to SARS-CoV-2 entry, there may also be quantitative differences in the overall efficiency of

497   viral replication in different cell types. Hou and colleagues previously hypothesised that post-entry

498   factors such as intrinsic antiviral immunity might dictate permissiveness. As discussed, we found

499   limited evidence to support such a correlation, since while virtually all nasal epithelial cells

500   demonstrated a basal ISG signature - consistent with *ex vivo* nasal biopsy data[10] - this was apparently

501   insufficient to mediate resistance to SARS-CoV-2, at least at the time point analysed. However, it

502   remains possible that cell-type specific differences in the efficiency of induction of the IFN response

503   (for example in basal cells) might contribute to more subtle variation in permissiveness.

504   The differential response of basal cell types to SARS-CoV-2 at 24 hpi identified by our scRNA-seq

505   analysis appears a novel observation. Basal cells are the stem/progenitor cell population of the

506   airway[67]. Recent data indicate an emerging role for these cells as sentinels of the airway inflammatory

507   response[68]. For example, basal cells detect apoptotic cells in the context of viral inflammation[69],

508   retaining memory of prior immune exposure[70]. More generally, stem/progenitor cell types exhibit

509   enhanced intrinsic antiviral immunity[71]. Future studies should consider mechanism(s) governing the

510   seemingly distinct early antiviral response of nasal airway basal cells to SARS-CoV-2, and its functional

511   relevance.

512   Importantly, from a clinical perspective, the observation that IFN-I/III treatment prevented SARS-CoV-

513   2 infection *in vitro* indicates that chemoprophylaxis with IFN-I/III may have therapeutic value. This

514   approach has already been tested in a small clinical trial in China (although the absence of a control

515   group makes it impossible to judge the efficacy of this approach[72]). Immunisation is the most tractable

516   approach for large-scale primary prevention of COVID-19. However, owing to incomplete vaccine

517   coverage, and reduced vaccine effectiveness in immunocompromised populations or against mildly

518   symptomatic or asymptomatic infection, allied to the emergence of variants that may compromise

519   vaccine efficacy, there will likely continue to be a need for targeted chemoprophylactic therapies to

520   prevent transmission in specific circumstances. These include post-exposure prophylaxis of contacts -

521   to avoid the need for self-isolation - as well as pre-exposure prophylaxis for certain high-risk

522   encounters (e.g. in healthcare settings or prior to long-distance travel). Our data suggest that nasal

523   application of IFNβ or IFNλ1 might have an important role to play in this setting and argue for urgent

524   clinical assessment of this approach. In terms of the therapeutic efficacy of mucosally-administered

525   IFNβ in patients with established COVID-19[41], our findings suggest that early administration may be a

526   key factor determining clinical efficacy. Furthermore, studies in animal models indicate that

527   administration of IFNβ or IFNλ1 later in the disease course may have deleterious effects on viral

528   inflammation and/or airway cell regeneration[73-75], suggesting the existence of a relatively narrow

529   therapeutic window of opportunity.

530   In summary, we have shown that SARS-CoV-2 exhibits broad tropism for nasal epithelial cells, but with

531   preferential infection of ciliated and secretory cell types. Nasal cells mount a robust innate antiviral

532   response to SARS-CoV-2 dominated by paracrine IFN-I/III signalling, which is delayed in onset relative

533   to viral replication, but which is nevertheless capable of exerting partial control at later times post-

534   infection. Upon exposure to exogenous IFN-I/III treatment, these cells adopt a profound antiviral

535   state, highlighting a potential clinical role for recombinant IFNβ or IFNλ1 in chemoprophylaxis and/or

536   therapy of COVID-19.

537

538   **METHODS**

539   **Adult nasal airway epithelial cell culture at air-liquid interface (ALI)**

540   Adult primary human nasal airway epithelial cells were derived from excess clinical material obtained

541   during routine nasal surgical procedures[29]. Ethical approval for sample collection was provided

542   (Research Ethics Committee Reference 17/NE/0361) and written approved consent was provided

543   prior to sample collection. Tissue shaved from the superficial surface of the sample was chopped into

544   ~2 mm^2 pieces and added to RPMI-1640 basal medium containing 0.1% protease (Sigma-Aldrich, UK)

545   and incubated overnight with gentle agitation at 4°C. All large pieces of tissue were discarded, and

546   residual protease was neutralized with 5% FCS. The preparation was centrifuged (200 g; 7 min) and

547   the pellet resuspended in PneumaCult-Ex Plus expansion medium (Stemcell Technologies), then

548   seeded onto 25 cm^2 tissue culture flasks pre-coated with 30 µg/mL Type I collagen (PureCol, Advanced

549   BioMatrix). Flasks were incubated in a humidified atmosphere containing 5% CO2 at 37°C, with

550   medium replaced every 48 hours. Cells were trypsinised at 60-80% confluence and cryopreserved for

551   future use. Upon thawing, cells were grown through an additional expansion phase, then transferred

552   in Ex Plus medium onto collagen-coated 6.5 mm polyester transwell membranes with 0.4 µm pore

553   size (Corning) at a density of 150,000 cells/cm^2. When cells were fully confluent, apical medium was

554   removed and basolateral medium was switched to PneumaCult-ALI-S (Stemcell Technologies). Cells

555   were maintained at air-liquid interface until fully differentiated. Barrier integrity of ALI cultures was

556   monitored by measuring trans-epithelial electrical resistance (TEER, EVOM 2, World Precision

557   Instruments). ALI cultures were validated for use in experiments based on microscopic appearance of

558   appropriate ciliated morphology and TEER > 500 Ω*cm^2. The sex and age of donors are included in

559   Table S4.

560

561   **Viruses, cytokines and inhibitors**

562   A clinical isolate of SARS-CoV-2 (BetaCoV/England/2/2020) was obtained from Public Health England

563   (PHE). This was isolated from a patient in January 2020 and thus represents an early strain of SARS-

564   CoV-2, not known to be affected by variants of concern. The initial stock was propagated once in vero

565   E6 cells. The same viral stock was used for all experiments. As SARS-CoV-2 is a Hazard Group 3

566   pathogen (Advisory Committee on Dangerous Pathogens, UK), all infection experiments were

567   performed in a dedicated Containment Level 3 (CL3) facility by trained personnel. Sendai virus (Cantell

568   strain) and parainfluenza virus 3 (PIV3) was obtained from Richard Randall (St Andrew's University).

569   Influenza A virus (A/PR8/1934/H1N1) was propagated and titred on MDCK cells. For nasal ALI

570   infections, apical poles were gently washed once with warm Dulbecco's modified Eagle's medium

571   (DMEM; Gibco, USA) and then infected with 60 µL dilution of virus in DMEM, at a MOI between 2 and

572   0.01 plaque-forming units per cell for 2 hours, when the virus-containing medium was removed.

573   DMEM was used as inoculum for mock infection. Apical washes (in warm phosphate-buffered saline)

574   were collected at different time points and stored at -80°C for plaque assays. Plaque assays were

575   undertaken in vero E6 cells using a 1.2% (w/v) microcrystalline cellulose overlay (Sigma-Aldrich).

576   Cytokines/inhibitors were used at the following concentrations: human recombinant IFNβ1 (1000

577   ng/mL; Avonex, NDC 59627-002-06, Biogen Inc, USA); IFNλ1 (100 ng/mL; 1598-IL-025, R&D Systems,

578   USA); and Ruxolitinib (10 µM; S1378, Calbiochem, USA) alongside the appropriate dilution of DMSO

579   vehicle. Treatment was applied through basolateral poles.

580

Single cell RNA sequencing (scRNA-seq) sample processing

For the droplet-encapsulation scRNA-seq experiments, ALI cultures were washed with PBS and then incubated with 1x Trypsin-EDTA (ThermoFisher Scientific, USA) for 10 min before the cells were diluted with DMEM and counted using a haemocytometer. 20,000 single cells were loaded onto each channel of a Chromium chip before encapsulation on the Chromium Controller (10x Genomics, USA). The single-cell sequencing libraries were generated using the Single Cell 5' V.1, as per the manufacturer's protocol. Libraries were sequenced using NovoSeq 6000 to achieve a minimum depth of 50,000 raw reads per cell. The libraries were sequenced using the following parameters: Read1: 26 cycles, i7: 8 cycles, i5: 0 cycles; Read2: 98 cycles to generate 75 bp paired-end reads.

590

Single-cell RNA sequencing (scRNA-seq) data generation and annotation

Sequencing data were demultiplexed and quantified using the Cellranger tool (version 4.0.0, 10x Genomics) and aligned to the combined human (official Cell Ranger reference, GRCh38-2020-A) and SARS-CoV-2 reference transcriptomes (Ensembl reference Sars_cov_2.ASM985889v3). CellBender (version 0.2.0)[76] was applied to the output from Cell Ranger software after alignment to remove background effect from ambient mRNA released during processing. Doublet detection and exclusion was performed using Scrublet (version 0.2.1) with thresholding of cells with a doublet score above two median absolute deviations from the median. Low-quality cells were removed using thresholds of < 200 genes and > 20% mitochondrial content. The analysis was performed using Seurat (version 4.0.1). Data were normalised and log-transformed using NormalizeData and the top 2000 variable genes identified using the FindVariableFeatures tool. The first 20 principal components were batch-adjusted using Harmony (by sample ID) and used to generate the nearest-neighbour graph. Dimensionality reduction and embedding was performed using Uniform Manifold Approximation and Projection (UMAP), with the neighbourhood graph clustered using the Leiden algorithm. The Wilcoxon rank sum test ($\log_2$ fold change threshold of 0.25, adjusted P value of 0.05) was used to identify

606   differentially expressed genes between clusters, and these were annotated based on expression of

607   markers from literature. This annotation was validated by comparing to a recently published scRNA-

608   seq dataset from ex vivo primary nasal cells[15]. The Seurat label transfer tool was used to assign

609   predicted identities to our data using the external published data as reference. The robustness of our

610   annotation was then assessed by the strength of its correlation with this prediction.

611

612   **Gene set scoring and gene set enrichment analysis**

613   A published gene set derived from IFN alpha or IFN gamma-treated human nasal basal cells[11] was used

614   to generate a list of epithelial-specific IFN-stimulated genes (ISGs). To calculate basal expression of

615   ISGs within the unexposed cells, over-expression of this gene list was assessed using the Seurat

616   AddModuleScore tool. Differences between clusters was compared by a Wilcoxon rank sum test

617   (adjusted alpha 0.05) with Benjamini-Hochburg multiple test correction applied.

618   Gene set enrichment analysis was performed using the fgsea tool[77]. Genes were ordered between

619   mock-infected and infected cells by fold-change in expression with Wilcoxon rank sum testing using

620   the FindAllMarkers function in Seurat, but without thresholds. Gene sets from Hallmark, Reactome

621   and Biocarta were used as reference after filtering to exclude those with fewer than 50 and greater

622   than 200 genes. Output from fgsea was further filtered to remove pathways that were not significantly

623   enriched in any cell type (adjusted P value <0.05) followed by further manual curation of the resultant

624   pathways.

625

626   **Regulon scoring and analysis**

627   The DoRoTHea/Viper package in R was used to score regulon activity by cell[78]. Human regulons from

628   DoRoTHea were filtered for those with a confidence score A-C. Normalised enrichment scores (NES)

629   for each transcription factor (TF) were calculated using run_viper with a minimum regulon size of 4 on

630   the complete gene expression matrix. To estimate TF activity over baseline within each cell type in the

631   infected cells, the median NES from the mock-infected clusters was subtracted from the equivalent in

632   the infected cluster. These scores were then scaled within each TF to give comparative estimate of TF

633   activity between clusters.

634

635   **Quantitative RT-PCR**

636   Total RNA was isolated using TRIzol^{TM} reagent (Invitrogen, Carlsbad, CA, USA) according to the

637   manufacturer's instructions. For qPCR analyses of transcripts, 250 ng of RNA isolated from the nasal

638   epithelial cells was reverse transcribed with Superscript III (ThermoFisher Scientific), and the resulting

639   cDNA templates were subjected to qPCR with a TaqMan^{TM} Gene Expression Master Mix (Applied

640   Biosystems, MA, USA) and AriaMx real-time PCR system (Agilent Technologies, CA, USA) according to

641   the manufacturer's instructions. The following TaqMan gene expression assays (Thermo Fischer) were

642   used: *IFNA1* (Hs03044218_g1), *TNF* (Hs00174128_m1). The primers were designed using the Roche

643   Universal Probe Library (UPL) Assay Design tool (Roche, Basel, Switzerland) with the indicated UPL

644   probes. All other primer and probe information is described in Table S5. Cycling conditions were as

645   follows: reverse transcription at 50°C for 15 min, followed by initial polymerase activation at 95°C for

646   10 min, then 40 cycles of denaturation at 95°C for 15 sec and annealing/extension at 60°C for 1 min.

647   The $2^{-\Delta\Delta Ct}$ method was used to calculate the relative expression of genes. Each sample was run in

648   duplicate. Samples were normalised to the endogenous housekeeping gene expression, either

649   *RNASEP* for *N* gene expression, or *18S* for all other genes.

650

651   **Immunofluorescence**

652   Immunofluorescence analysis was performed in accordance with published methods[79]. Infected and

653   mock-infected membranes were fixed *in situ* with 4% (w/v) paraformaldehyde overnight at 4°C, before

654   removal from transwells and sectioning. Membranes were washed twice for 5 min in PBS plus 0.1%

655   (v/v) Triton X-100 (Sigma-Aldrich) before being blocked with a 1% (w/v) BSA solution in PBS with 0.5%

656   (v/v) Tween 20 (Sigma-Aldrich; PBST) for one hour at room temperature (RT). Membranes were

657   incubated with primary antibodies for 2 hours at RT. Antibodies used are listed in Table S6.

658   Membranes were washed three times for 5 min in PBST before incubation with appropriate

659   fluorescence-conjugated secondary antibodies for 2 hours at RT. This process was repeated as part of

660   a sequential staining process where required. Membranes were washed three times for 5 min in PBST

661   before being incubated with DAPI (50 nM; Sigma-Aldrich) as a nuclear counterstain, and phalloidin,

662   DyLight 650 (1 unit/mL; ThermoFisher) where required, for 10 min. Membranes were then mounted

663   in MOWIOL mounting media (Sigma-Aldrich) and coverslips applied. Appropriate secondary only

664   controls were performed as required. Images were captured using a Nikon A1 confocal microscope

665   (Nikon, Japan), with all capture settings standardised. For analysis three random fields per sample

666   were captured at x20 magnification and analysed via Fiji (Version 2.0) using the Cell Counter plugin.

667   Total cell count, and number of spike protein-positive cells, were determined by segmenting images

668   using ZO-1 and DAPI to identify individual cells. Mean pixel intensity of the spike protein in positive

669   cells was also determined using the Plot Profile plugin.

670

671   **Immunoblot**

672   Immunoblotting was carried out as previously described[40]. Briefly, proteins from cell lysates were

673   separated by 10% sodium dodecyl sulphate polyacrylamide gel electrophoresis (SDS-PAGE) using

674   MOPS running buffer (Thermo Fisher, USA), and transferred to a nitrocellulose membrane (Millipore,

675   USA) using NuPage Tris-Bis Transfer Buffer (Thermo Fisher) for immunoblotting (for details of

676   antibodies see Table S6). Blots were developed with Pierce ECL Western blotting substrate (Thermo

677   Fisher) and imaged on a LI-COR Odyssey Fc (LI-COR, USA). Densitometry was undertaken using

678   ImageStudio software (LI-COR).

679

680   **Transmission electron microscopy (TEM)**

681   Cultures were fixed with 2% glutaraldehyde (Sigma-Aldrich, MO, USA) in 0.1 M sodium cacodylate (pH

682   7.4) buffer in the apical and basal compartment and then kept at 4°C overnight. For TEM resin

683   processing, the monolayer membranes were removed from the insert frame and placed in microwave

684   sample holders. The Pelco Biowave Pro+ microwave (Pelco, CA, USA), incorporating the Pelco ColdSpot

685   Pro system, was used for the following steps of the processing. The ColdSpot system

686   improves inconsistent wattage supply to the microwave compartment, therefore protecting samples

687   from excess microwave energy. The range temperature was set at 23–27°C. Following buffer rinses

688   (three pulses at 150 watts (W) for 40 secs) the samples were post-fixed in 1% osmium tetroxide for 8

689   min [pulse microwaved (MW), 100 W] and rinsed in distilled H_2O (three times at 150 W for 40 secs,

690   per step). Samples were dehydrated in a graded series of acetone (25%; 50%; 75%; three times with

691   100% (v/v); 150 W, 40 secs per step) before being impregnated with increasing concentrations of

692   epoxy resin (medium resin; TAAB, UK) in acetone (25%; 50%; 75%; three times at 100% (v/v); 300 W,

693   3 min per step). The samples were then embedded in 100% fresh resin and left to polymerise at 60°C

694   in a conventional oven for a minimum of 24 hours. All resin blocks were trimmed using a razor blade

695   to form a trapezoid block face. Sections were cut on an ultramicrotome using a diamond knife. Semi

696   thin sections (0.5 μm) were stained with toluidine blue and viewed on a light microscope to verify

697   presence of cell monolayers. Ultrathin sections (70 nm) were then cut and picked up onto pioloform-

698   coated copper grids. Grids were stained with 1% (w/v) uranyl acetate (30 min) and 3% (w/v) lead

699   citrate (7 min) to improve contrast. All sections were examined using a HT7800 120 kV TEM (Hitachi,

700   Japan). Digital micrographs were captured using an EMSIS Xarosa CMOS Camera with Radius software

701   (EMSIS, Germany). ImageJ software (Version 2.0) was used to enhance the contrast by increasing the

702   percentage of saturated pixels to 1% to aid virus-like particle identification. Virus-like particles

703   (~70 nm in diameter) were counted using the cell counter plugin in at least 6 goblet cells and 16

704   ciliated cells per donor. Data were presented as number of virus-like particles per cell.

705

706   **Proteome sample preparation**

707   The protein concentration was determined by EZQ® protein quantification assay. Protein digestion was

708   performed using the S-Trap™ sample preparation method and TMT-16 plex labelling was carried out

709   as per the manufacturer's instructions. Samples were cleaned using MacroSpin columns, and dried

710   down prior to offline high-performance liquid chromatography fractionation. Peptides were

711   fractionated on a Basic Reverse Phase column on a Dionex Ultimate 3000 off-line LC system. A total of

712   18 fractions were collected, and each fraction was acidified and dried. Peptides were dissolved in 5%

713   formic acid, and each sample was independently analysed on an Orbitrap Fusion Lumos Tribrid mass

714   spectrometer, connected to an UltiMate 3000 RSLCnano System. All spectra were analysed using

715   MaxQuant 1.6.10.43 and searched against SwissProt *Homo sapiens* and Trembl SARS-CoV-2 FASTA

716   files. Reporter ion MS3 was used for quantification and the additional parameter of quantitation labels

717   with 16 plex TMT on N-terminus or lysine was included. A protein and peptide false discovery rate

718   (FDR) of less than 1% was employed in MaxQuant. Moderated t-tests, with patient accounted for in

719   the linear model, was performed using Limma, where proteins with an adjusted $P < 0.05$ were

720   considered as statistically significant. All analysis was performed using R. Raw data are present in

721   supplementary dataset 5. A comprehensive description of the methods can be found in the

722   supplementary methods.

723

724   **Statistical analysis**

725   Statistical analysis was performed and figures assembled using GraphPad Prism V9 (GraphPad

726   Software, USA). Data are presented as mean ± SEM of individual donor values (derived typically from

727   2-3 independent repeat experiments per donor). The donor was used as the unit of experiment for

728   statistical analysis purposes. Continuous data were normalised or log-transformed prior to analysis

729   using parametric significance tests, or if this was not possible, were analysed using nonparametric

730   significance tests. Differences between two groups were compared using an unpaired, two-tailed

731   Student's t-test (or Mann-Whitney test for TEM image analysis), whereas differences between more

732   than two groups used ANOVA, with Dunnett's post-test correction for multiple comparisons when

733   comparing to a single reference point (e.g. mock-infected or time zero) or with Sidak's post-test

734   correction for other multiple comparisons (e.g. between differently treated donors at the same time

735   point). In some cases, data were normalised to a reference point, where a one-sample t-test was used.

736   Unless stated otherwise, a two-tailed alpha of < 0.05 was the threshold for statistical significance.

737   Statistical analysis of proteomics and transcriptomics data sets is described in the relevant sections

738   above.

739

740   **Data availability**

741   Source data are provided with this paper. This includes uncropped blots, all quantitative data and the

742   results of differential expression analysis of RNA-seq and proteomics data, which are included as

743   supplementary datasets. Additional raw data are available on request from the corresponding author

744   providing ethical approvals permit sharing of data. The mass spectrometry proteomics data have been

745   deposited to the ProteomeXchange Consortium[80] via the PRIDE partner repository[81] with the dataset

746   identifier PXD022523. This can be accessed through the Username: reviewer_pxd022523@ebi.ac.uk

747   and the Password: UaEXYFKF. Raw RNA sequencing data have been deposited to the European

748   Genome-Phenome Archive (accession pending). Processed scRNAseq data is available at Zenodo

749   (https://zenodo.org/record/4564332).

750

751   **Code availability**

752   Analysis scripts and codes are available at github.com/haniffalab/covid_nasal_epithelium.

753

754   **Acknowledgements**

776

777   **Author contributions**

778   Conceived the study: MB, CW, CJAD with MH, SH, MT. Experimental design: MH, SH, MB, CW, MT, GR,

779   CJAD. Nasal model development and patient material: IJH, BV, JS, JPG, SC, JP, AJS, MB, CW. Virology

780   data generation, analysis and interpretation: CFH, BJT, JSS, FG, AIG, AK, LH, TD, SH, CJAD. Proteomics

781   data generation, analysis and interpretation: MED, SM, MT. Single-cell sequencing data generation,

782   analysis and interpretation: RAB, ES, RH, JC, MH, GR. Supervised research: AJS, MH, SH, MB, CW, MT,

783   GR, CJAD. Drafted the manuscript: CFH and CJAD with ES, BV, MED, TD, MT, GR. Revised the

784   manuscript: RAB, MED, IJH, JSS, AJS, MH, SH, CW. Approved the manuscript for submission: all

785   authors.

786

787   **Declaration of competing interests**

788   SH declares honoraria from CSL Behring and Takeda for teaching and consultancy. The remaining

789   authors declare no financial or non-financial competing interests.

790   **References**

791   1   Zhu, N. *et al.* A Novel Coronavirus from Patients with Pneumonia in China, 2019. *N*
792   *Engl J Med* **382**, 727-733, doi:10.1056/NEJMoa2001017 (2020).
793   2   Hoffmann, M. *et al.* SARS-CoV-2 Cell Entry Depends on ACE2 and TMPRSS2 and Is
794   Blocked by a Clinically Proven Protease Inhibitor. *Cell* **181**, 271-280 e278,
795   doi:10.1016/j.cell.2020.02.052 (2020).
796   3   Huang, C. *et al.* Clinical features of patients infected with 2019 novel coronavirus in
797   Wuhan, China. *Lancet* **395**, 497-506, doi:10.1016/S0140-6736(20)30183-5 (2020).
798   4   Knight, S. R. *et al.* Risk stratification of patients admitted to hospital with covid-19
799   using the ISARIC WHO Clinical Characterisation Protocol: development and validation
800   of the 4C Mortality Score. *BMJ* **370**, m3339, doi:10.1136/bmj.m3339 (2020).
801   5   Group, R. C. *et al.* Dexamethasone in Hospitalized Patients with Covid-19 - Preliminary
802   Report. *N Engl J Med*, doi:10.1056/NEJMoa2021436 (2020).
803   6   Group, R. C. Tocilizumab in patients admitted to hospital with COVID-19 (RECOVERY):
804   a randomised, controlled, open-label, platform trial. *Lancet* **397**, 1637-1645,
805   doi:10.1016/S0140-6736(21)00676-0 (2021).
806   7   Cevik, M., Kuppalli, K., Kindrachuk, J. & Peiris, M. Virology, transmission, and
807   pathogenesis of SARS-CoV-2. *BMJ* **371**, m3862, doi:10.1136/bmj.m3862 (2020).
808   8   Chen, M. *et al.* Elevated ACE-2 expression in the olfactory neuroepithelium:
809   implications for anosmia and upper respiratory SARS-CoV-2 entry and replication. *Eur*
810   *Respir J* **56**, doi:10.1183/13993003.01948-2020 (2020).
811   9   Hoagland, D. A. *et al.* Leveraging the antiviral type I interferon system as a first line of
812   defense against SARS-CoV-2 pathogenicity. *Immunity*,
813   doi:10.1016/j.immuni.2021.01.017 (2021).
814   10   Sungnak, W. *et al.* SARS-CoV-2 entry factors are highly expressed in nasal epithelial
815   cells together with innate immune genes. *Nat Med* **26**, 681-687, doi:10.1038/s41591-
816   020-0868-6 (2020).
817   11   Ziegler, C. G. K. *et al.* SARS-CoV-2 Receptor ACE2 Is an Interferon-Stimulated Gene in
818   Human Airway Epithelial Cells and Is Detected in Specific Cell Subsets across Tissues.
819   *Cell* **181**, 1016-1035 e1019, doi:10.1016/j.cell.2020.04.035 (2020).
820   12   Gamage, A. M. *et al.* Infection of human Nasal Epithelial Cells with SARS-CoV-2 and a
821   382-nt deletion isolate lacking ORF8 reveals similar viral kinetics and host
822   transcriptional profiles. *PLoS Pathog* **16**, e1009130,
823   doi:10.1371/journal.ppat.1009130 (2020).
824   13   Hou, Y. J. *et al.* SARS-CoV-2 Reverse Genetics Reveals a Variable Infection Gradient in
825   the Respiratory Tract. *Cell* **182**, 429-446 e414, doi:10.1016/j.cell.2020.05.042 (2020).
826   14   Pizzorno, A. *et al.* Characterization and Treatment of SARS-CoV-2 in Nasal and
827   Bronchial Human Airway Epithelia. *Cell Rep Med* **1**, 100059,
828   doi:10.1016/j.xcrm.2020.100059 (2020).
829   15   Ziegler, C. G. K. *et al.* Impaired local intrinsic immunity to SARS-CoV-2 infection in
830   severe COVID-19. *Cell*, doi:10.1016/j.cell.2021.07.023 (2021).
831   16   Onabajo, O. O. *et al.* Interferons and viruses induce a novel truncated ACE2 isoform
832   and not the full-length SARS-CoV-2 receptor. *Nat Genet* **52**, 1283-1293,
833   doi:10.1038/s41588-020-00731-9 (2020).

834   17   Duncan, C. J. A., Randall, R. E. & Hambleton, S. Genetic Lesions of Type I Interferon
835   Signalling in Human Antiviral Immunity. *Trends Genet* **37**, 46-58,
836   doi:10.1016/j.tig.2020.08.017 (2021).
837   18   Zhang, Q. *et al.* Inborn errors of type I IFN immunity in patients with life-threatening
838   COVID-19. *Science* **370**, doi:10.1126/science.abd4570 (2020).
839   19   Pairo-Castineira, E. *et al.* Genetic mechanisms of critical illness in Covid-19. *Nature*,
840   doi:10.1038/s41586-020-03065-y (2020).
841   20   Bastard, P. *et al.* Autoantibodies against type I IFNs in patients with life-threatening
842   COVID-19. *Science* **370**, doi:10.1126/science.abd4585 (2020).
843   21   Lokugamage, K. G. *et al.* Type I Interferon Susceptibility Distinguishes SARS-CoV-2
844   from SARS-CoV. *J Virol* **94**, doi:10.1128/JVI.01410-20 (2020).
845   22   Felgenhauer, U. *et al.* Inhibition of SARS-CoV-2 by type I and type III interferons. *J Biol*
846   *Chem* **295**, 13958-13964, doi:10.1074/jbc.AC120.013788 (2020).
847   23   Lee, J. S. & Shin, E. C. The type I interferon response in COVID-19: implications for
848   treatment. *Nat Rev Immunol* **20**, 585-586, doi:10.1038/s41577-020-00429-3 (2020).
849   24   Zhu, N. *et al.* Morphogenesis and cytopathic effect of SARS-CoV-2 infection in human
850   airway epithelial cells. *Nat Commun* **11**, 3910, doi:10.1038/s41467-020-17796-z
851   (2020).
852   25   Fiege, J. K. *et al.* Single cell resolution of SARS-CoV-2 tropism, antiviral responses, and
853   susceptibility to therapies in primary human airway epithelium. *PLoS Pathog* **17**,
854   e1009292, doi:10.1371/journal.ppat.1009292 (2021).
855   26   Vanderheiden, A. *et al.* Type I and Type III Interferons Restrict SARS-CoV-2 Infection of
856   Human Airway Epithelial Cultures. *J Virol* **94**, doi:10.1128/JVI.00985-20 (2020).
857   27   Blanco-Melo, D. *et al.* Imbalanced Host Response to SARS-CoV-2 Drives Development
858   of COVID-19. *Cell* **181**, 1036-1045 e1039, doi:10.1016/j.cell.2020.04.026 (2020).
859   28   Huang, J. *et al.* SARS-CoV-2 Infection of Pluripotent Stem Cell-derived Human Lung
860   Alveolar Type 2 Cells Elicits a Rapid Epithelial-Intrinsic Inflammatory Response.
861   *bioRxiv*, doi:10.1101/2020.06.30.175695 (2020).
862   29   Mavin, E. *et al.* Real-time measurement of cellular bioenergetics in fully differentiated
863   human nasal epithelial cells grown at air-liquid-interface. *Am J Physiol Lung Cell Mol*
864   *Physiol* **318**, L1158-L1164, doi:10.1152/ajplung.00414.2019 (2020).
865   30   Vieira Braga, F. A. *et al.* A cellular census of human lungs identifies novel cell states in
866   health and in asthma. *Nat Med* **25**, 1153-1163, doi:10.1038/s41591-019-0468-5
867   (2019).
868   31   Ruiz Garcia, S. *et al.* Novel dynamics of human mucociliary differentiation revealed by
869   single-cell RNA sequencing of nasal epithelial cultures. *Development* **146**,
870   doi:10.1242/dev.177428 (2019).
871   32   Xiu, S. *et al.* Inhibitors of SARS-CoV-2 Entry: Current and Future Opportunities. *J Med*
872   *Chem* **63**, 12256-12274, doi:10.1021/acs.jmedchem.0c00502 (2020).
873   33   Prelli Bozzo, C. *et al.* IFITM proteins promote SARS-CoV-2 infection and are targets for
874   virus inhibition in vitro. *Nat Commun* **12**, 4584, doi:10.1038/s41467-021-24817-y
875   (2021).
876   34   Li, S. *et al.* Metabolic reprogramming and epigenetic changes of vital organs in SARS-
877   CoV-2-induced systemic toxicity. *JCI Insight* **6**, doi:10.1172/jci.insight.145027 (2021).
878   35   Moolamalla, S. T. R., Balasubramanian, R., Chauhan, R., Priyakumar, U. D. & Vinod, P.
879   K. Host metabolic reprogramming in response to SARS-CoV-2 infection: A systems

880   biology approach. *Microb Pathog* **158**, 105114, doi:10.1016/j.micpath.2021.105114
881   (2021).
882 36 Ravindra, N. G. *et al.* Single-cell longitudinal analysis of SARS-CoV-2 infection in human
883   airway epithelium identifies target cells, alterations in gene expression, and cell state
884   changes. *PLoS Biol* **19**, e3001143, doi:10.1371/journal.pbio.3001143 (2021).
885 37 Lei, X. *et al.* Activation and evasion of type I interferon responses by SARS-CoV-2. *Nat*
886   *Commun* **11**, 3810, doi:10.1038/s41467-020-17665-9 (2020).
887 38 Cardoso, R. S. *et al.* Host Retromer Protein Sorting Nexin 2 Interacts with Human
888   Respiratory Syncytial Virus Structural Proteins and is Required for Efficient Viral
889   Production. *mBio* **11**, doi:10.1128/mBio.01869-20 (2020).
890 39 Bergant Marusic, M., Ozbun, M. A., Campos, S. K., Myers, M. P. & Banks, L. Human
891   papillomavirus L2 facilitates viral escape from late endosomes via sorting nexin 17.
892   *Traffic* **13**, 455-467, doi:10.1111/j.1600-0854.2011.01320.x (2012).
893 40 Duncan, C. J. A. *et al.* Severe type I interferonopathy and unrestrained interferon
894   signaling due to a homozygous germline mutation in STAT2. *Sci Immunol* **4**,
895   doi:10.1126/sciimmunol.aav7501 (2019).
896 41 Monk, P. D. *et al.* Safety and efficacy of inhaled nebulised interferon beta-1a (SNG001)
897   for treatment of SARS-CoV-2 infection: a randomised, double-blind, placebo-
898   controlled, phase 2 trial. *Lancet Respir Med*, doi:10.1016/S2213-2600(20)30511-7
899   (2020).
900 42 Antonelli, G. *et al.* Type I interferons can be detected in respiratory swabs from SARS-
901   Cov-2 infected patients. *J Clin Virol* **128**, 104450, doi:10.1016/j.jcv.2020.104450
902   (2020).
903 43 Cheemarla, N. R. *et al.* Dynamic innate immune response determines susceptibility to
904   SARS-CoV-2 infection and early replication kinetics. *J Exp Med* **218**,
905   doi:10.1084/jem.20210583 (2021).
906 44 Mick, E. *et al.* Upper airway gene expression reveals suppressed immune responses to
907   SARS-CoV-2 compared with other respiratory viruses. *Nat Commun* **11**, 5854,
908   doi:10.1038/s41467-020-19587-y (2020).
909 45 Rebendenne, A. *et al.* SARS-CoV-2 triggers an MDA-5-dependent interferon response
910   which is unable to control replication in lung epithelial cells. *J Virol*,
911   doi:10.1128/JVI.02415-20 (2021).
912 46 Sampaio, N. G. *et al.* The RNA sensor MDA5 detects SARS-CoV-2 infection. *Sci Rep* **11**,
913   13638, doi:10.1038/s41598-021-92940-3 (2021).
914 47 Yin, X. *et al.* MDA5 Governs the Innate Immune Response to SARS-CoV-2 in Lung
915   Epithelial Cells. *Cell Rep* **34**, 108628, doi:10.1016/j.celrep.2020.108628 (2021).
916 48 Kumar, A. *et al.* SARS-CoV-2 Nonstructural Protein 1 Inhibits the Interferon Response
917   by Causing Depletion of Key Host Signaling Factors. *J Virol* **95**, e0026621,
918   doi:10.1128/JVI.00266-21 (2021).
919 49 Wolff, G., Melia, C. E., Snijder, E. J. & Barcena, M. Double-Membrane Vesicles as
920   Platforms for Viral Replication. *Trends Microbiol* **28**, 1022-1033,
921   doi:10.1016/j.tim.2020.05.009 (2020).
922 50 Finkel, Y. *et al.* SARS-CoV-2 uses a multipronged strategy to impede host protein
923   synthesis. *Nature* **594**, 240-245, doi:10.1038/s41586-021-03610-3 (2021).
924 51 Schubert, K. *et al.* SARS-CoV-2 Nsp1 binds the ribosomal mRNA channel to inhibit
925   translation. *Nat Struct Mol Biol* **27**, 959-966, doi:10.1038/s41594-020-0511-8 (2020).

926   52   Thoms, M. *et al.* Structural basis for translational shutdown and immune evasion by
927   the Nsp1 protein of SARS-CoV-2. *Science* **369**, 1249-1255,
928   doi:10.1126/science.abc8665 (2020).
929   53   Hsu, J. C., Laurent-Rolle, M., Pawlak, J. B., Wilen, C. B. & Cresswell, P. Translational
930   shutdown and evasion of the innate immune response by SARS-CoV-2 NSP14 protein.
931   *Proc Natl Acad Sci U S A* **118**, doi:10.1073/pnas.2101161118 (2021).
932   54   Robinot, R. *et al.* SARS-CoV-2 infection induces the dedifferentiation of multiciliated
933   cells and impairs mucociliary clearance. *Nat Commun* **12**, 4354, doi:10.1038/s41467-
934   021-24521-x (2021).
935   55   Galani, I. E. *et al.* Untuned antiviral immunity in COVID-19 revealed by temporal type
936   I/III interferon patterns and flu comparison. *Nat Immunol* **22**, 32-40,
937   doi:10.1038/s41590-020-00840-x (2021).
938   56   Hadjadj, J. *et al.* Impaired type I interferon activity and inflammatory responses in
939   severe COVID-19 patients. *Science* **369**, 718-724, doi:10.1126/science.abc6027 (2020).
940   57   Stephenson, E. *et al.* Single-cell multi-omics analysis of the immune response in
941   COVID-19. *Nat Med* **27**, 904-916, doi:10.1038/s41591-021-01329-2 (2021).
942   58   Lopez, J. *et al.* Early nasal type I IFN immunity against SARS-CoV-2 is compromised in
943   patients with autoantibodies against type I IFNs. *J Exp Med* **218**,
944   doi:10.1084/jem.20211211 (2021).
945   59   Molony, R. D. *et al.* Aging impairs both primary and secondary RIG-I signaling for
946   interferon induction in human monocytes. *Sci Signal* **10**,
947   doi:10.1126/scisignal.aan2392 (2017).
948   60   Loske, J. *et al.* Pre-activated antiviral innate immunity in the upper airways controls
949   early SARS-CoV-2 infection in children. *Nat Biotechnol*, doi:10.1038/s41587-021-
950   01037-9 (2021).
951   61   Purkayastha, A. *et al.* Direct Exposure to SARS-CoV-2 and Cigarette Smoke Increases
952   Infection Severity and Alters the Stem Cell-Derived Airway Repair Response. *Cell Stem
953   Cell* **27**, 869-875 e864, doi:10.1016/j.stem.2020.11.010 (2020).
954   62   Hartmann, E. *et al.* Analysis of plasmacytoid and myeloid dendritic cells in nasal
955   epithelium. *Clin Vaccine Immunol* **13**, 1278-1286, doi:10.1128/CVI.00172-06 (2006).
956   63   Onodi, F. *et al.* SARS-CoV-2 induces human plasmacytoid pre-dendritic cell
957   diversification via UNC93B and IRAK4. *bioRxiv*, doi:10.1101/2020.07.10.197343
958   (2021).
959   64   Cervantes-Barragan, L. *et al.* Plasmacytoid dendritic cells produce type I interferon and
960   reduce viral replication in airway epithelial cells after SARS-CoV-2 infection. *bioRxiv*,
961   doi:10.1101/2021.05.12.443948 (2021).
962   65   Pierce, C. A. *et al.* Natural mucosal barriers and COVID-19 in children. *JCI Insight* **6**,
963   doi:10.1172/jci.insight.148694 (2021).
964   66   Ziegler, C. G. K. *et al.* Impaired local intrinsic immunity to SARS-CoV-2 infection in
965   severe COVID-19. *bioRxiv*, doi:10.1101/2021.02.20.431155 (2021).
966   67   Rock, J. R. *et al.* Basal cells as stem cells of the mouse trachea and human airway
967   epithelium. *Proc Natl Acad Sci U S A* **106**, 12771-12775, doi:10.1073/pnas.0906850106
968   (2009).
969   68   Hewitt, R. J. & Lloyd, C. M. Regulation of immune responses by the airway epithelial
970   cell landscape. *Nat Rev Immunol* **21**, 347-362, doi:10.1038/s41577-020-00477-9
971   (2021).

69   Fujino, N. *et al.* Sensing of apoptotic cells through Axl causes lung basal cell proliferation in inflammatory diseases. *J Exp Med* **216**, 2184-2201, doi:10.1084/jem.20171978 (2019).

70   Ordovas-Montanes, J. *et al.* Allergic inflammatory memory in human respiratory epithelial progenitor cells. *Nature* **560**, 649-654, doi:10.1038/s41586-018-0449-8 (2018).

71   Wu, X. *et al.* Intrinsic Immunity Shapes Viral Resistance of Stem Cells. *Cell* **172**, 423-438 e425, doi:10.1016/j.cell.2017.11.018 (2018).

72   Meng, Z. *et al.* An experimental trial of recombinant human interferon alpha nasal drops to prevent COVID-19 in medical staff in an epidemic area. *MedRxiv*, doi:doi.org/10.1101/2020.04.11.20061473 (2020).

73   Boudewijns, R. *et al.* STAT2 signaling restricts viral dissemination but drives severe pneumonia in SARS-CoV-2 infected hamsters. *Nat Commun* **11**, 5838, doi:10.1038/s41467-020-19684-y (2020).

74   Major, J. *et al.* Type I and III interferons disrupt lung epithelial repair during recovery from viral infection. *Science* **369**, 712-717, doi:10.1126/science.abc2061 (2020).

75   Broggi, A. *et al.* Type III interferons disrupt the lung epithelial barrier upon viral recognition. *Science* **369**, 706-712, doi:10.1126/science.abc3545 (2020).

76   Fleming, S. J., Marioni, J. C. & Babadi, M. CellBender remove-background: a deep generative model for unsupervised removal of background noise from scRNA-seq datasets. *bioRxiv*, doi:10.1101/791699 (2019).

77   Korotkevich, G. *et al.* Fast gene set enrichment analysis. *bioRxiv*, doi:10.1101/060012 (2021).

78   Holland, C. H. *et al.* Robustness and applicability of transcription factor and pathway analysis tools on single-cell RNA-seq data. *Genome Biol* **21**, 36, doi:10.1186/s13059-020-1949-z (2020).

79   Crowe, A. R. & Yue, W. Semi-quantitative Determination of Protein Expression using Immunohistochemistry Staining and Analysis: An Integrated Protocol. *Bio Protoc* **9**, doi:10.21769/BioProtoc.3465 (2019).

80   Deutsch, E. W. *et al.* The ProteomeXchange consortium in 2017: supporting the cultural change in proteomics public data deposition. *Nucleic Acids Res* **45**, D1100-D1106, doi:10.1093/nar/gkw936 (2017).

81   Perez-Riverol, Y. *et al.* The PRIDE database and related tools and resources in 2019: improving support for quantification data. *Nucleic Acids Res* **47**, D442-D450, doi:10.1093/nar/gky1106 (2019).